Temperature measurement of the thermionic electron emitter

Savenije, Joran H.

Award date:
2020

Eindhoven University of Technology

Temperature Measurement of the Thermionic Electron Emitter

Joran Savenije

Supervisors:

ir. Wiebe Toonen
dr.ir. Peter Mutsaers
prof.dr.ir. Jom Luiten

CQT 2020 - 01 - 45 ECTS

Eindhoven, January 2020

Abstract

Electron injectors with a low beam emittance and a high repetition rate are used for developing next-generation light sources with a high average brightness. For the experiments in this report a 100 kV thermionic gun has been built that is capable of delivering a continuous electron current of 10 mA using a LaB_6 disk electron emitter and 1 mA using a tantalum disk electron emitter. The life of an thermionic electron emitter is largely determined by the operational temperature of the emitter and the pressure inside the vacuum vessel. Operating near the operational temperature limit is desired as it maximizes the beam current, while keeping emittance low. To maximize the output of the electron emitter, while maintaining stable operation below the threshold at which thermal life-limiting processes deteriorate the material structure, a dual wavelength pyrometry setup was developed that can be used during operation. This is a form of a non-contact temperature measurement, in which light emitted by the electron emitter was collected and sent to multiple detectors. The ratio of the intensities of 1050 nm and 1550 nm was used to determine the temperature of the electron emitter during operation. Using a single band of wavelengths instead of a ratio and a CCD camera have also been investigated as other methods to determine the temperature, but their uncertainties are higher with the current setup. Due to the high amount of radiation produced, the current was limited to 4 μA using the tantalum cathode. For the tantalum cathode with a diameter of 0.84 mm the temperature could be measured with an accuracy of 4.7 % at 2200 K using dual wavelength pyrometry. The error in the absolute temperature can be decreased when using a calibration setup that has been designed, but not yet built. The LaB_6 emitter has a diameter of 0.3 mm and is surrounded by a pyrolytic guard ring. Therefore the self made dual wavelength pyrometer needs to have a focus spot of 50 μm at a distance of more than 50 cm. The low signal, in the order of nA, and the chromatic aberrations of the lenses had a large effect on the alignment of the pyrometer setup and caused too much uncertainty. This method in combination with the LaB_6 emitter will therefore only be reliable when the setup is calibrated. The end goal of this project is to determine and stabilize the operational temperature of the LaB_6 emitter at 1760 K within an uncertainty of ± 40 K (2.27 %) in order to develop a 100 kV thermonic gun that is capable of delivering a continuous current of 10 mA, which is then chopped and compressed by RF cavities resulting in 279 fs, 2.0 pC electron bunches with an emittance of 0.089 mm mrad at a repetition rate of 1.5 GHz.

Contents

Chapter 1

Introduction

1.1 Motivation

Over the past decade, high brightness electron sources have enabled the development of a variety of radio-frequency (RF) accelerator-based devices, such as free electron lasers (FELs)[1] and inverse Compton scattering (ICS) light sources[2]. The brightness of an electron source is typically used to indicate the beam quality and is defined as the beam current per unit area per solid angle. It is related to the beam current and the emittance of the beam. The emittance is a measure for the average spread of particle coordinates in position and momentum phase space. The quality and properties of the x-ray beam largely depend on the electron gun performance[3]. For RF accelerator-based light sources, the electron beam needs to be bunched as a continuous beam cannot be accelerated with RF electric fields. Therefore the electron sources output high charge electron bunches at a certain repetition rate, resulting in a peak brightness when an electron bunch is released. In fact, the first generation FELs were successful mainly due to the high peak brightness performance of the electron guns, but operate at relatively low repetition rates of around 100 Hz[4]. In the last several years, developments of the aforementioned devices have resulted in the proposals for next generation x-ray sources asking for MHz and even GHz repetition rates. This has increased the demand for electron sources producing electron bunches with a high brightness as well as high repetition rates[5]. One of these proposals is a compact ICS scheme developed at the Eindhoven University of Technology, in which photons from a laser beam are turned into X-ray photons as they are bounced off a relativistic electron beam[6]. For this approach a pulsed 100 kV electron injector is needed that provides high brightness and high charge electron bunches that can be accelerated in an RF accelerator structure. In section 1.2 different high repetition rate electron gun schemes are discussed.

In this report the early stages of the development of a 100 kV high repetition rate thermionic electron gun are described. In the first stage the electron gun will be operated with a continuous electron beam with a current of 10 mA, a limit set by the power supply, while minimizing the emittance of the beam. A low emittance means that the electrons in the beam are confined to a small distance and have nearly the same momentum. To keep the beam emittance low, the electron gun has to be operated at a temperature close to its operational limit of 1800 K, at which the support structure of the emitter loses its structural strength and breaks. To achieve this, the temperature of the electron emitter inside the gun needs to be controlled precisely. For an operational temperature of 1760 K, this means controlled within the range of ± 40 K, which is equal to an error margin of 2.27 %. Preferably, the uncertainty window is smaller, in the range of ± 10 K, which means an error margin of 0.6 %. For the emission of the electrons a LaB_6 emitter will be used. To output an electron beam with a current of 10 mA at 1760 K, the required emitter area can be determined for a specific emitter material, LaB_6 in this case, using the Richardson's equation. This is described in section 2.1. It follows that an circular emitter with a radius of 150 µm is needed to achieve the lowest initial emittance within the operational limits. However, for test purposes, first a tantalum emitter will be used.

Chapter 2 starts with a description of thermionic emission in combination with the Schottky effect for different emitter materials in section 2.1. Section 2.2 explains the effect of the operational temperature

and the radius of the emitter on emission current and the thermal emittance. Then, in section 2.3 the theory behind black body radiation is explained and different methods that use black body radiation to determine the temperature are compared. Section 2.4 gives a qualitative description of the RF cavities that will be added in the future, as the RF cavities are crucial to succesful operation of this thermionic electron gun. The experimental setup as it is used for the experiments and the description of its components is shown in chapter 3, in which sections 3.1, 3.2 and 3.3 give an overview of the thermionic gun and the beamline, section 3.10 explains the main optical part of the setup used for the dual wavelenth pyrometry measurements. Section 3.6 and 3.7 explain a calibration setup design and discuss the setup of other methods aside from the dual wavelength pyrometry setup. The results of the other methods are shown in section 4.1 and the results of the temperature measurement using a custom built dual wavelength pyrometer are shown in section 4.2. Radiation during experiments is discussed in section 4.3. The conclusion can be found in chapter 5 and the outlook is given in chapter 6.

1.2 High repetition rate electron gun schemes

An electron gun produces a narrow collimated electron beam with a specific kinetic energy. The normal conducting (NC) radio-frequency (RF) electron guns operate at a repetition rate of several hundred Hz and cannot be scaled up to repetition rates higher than several kHz. The power density dissipated on the RF cavity walls of the gun would be too high in order to sustain the required accelerating fields and would cause the cavity walls to deform or melt[3]. The next generation light sources designed for operation at high peak intensity as well as high average intensity with short and low emittance electron pulses, require electron guns capable of producing bunches with charges over 50 pC and a normalized emittance below 0.5 mm mrad in x- and y-direction, taking z as the propagation direction of the beam, at repetition rates of MHz or higher[7].

There are several approaches to create a high repetition rate electron gun. The three different ways this is currently being done are using a very high frequency (VHF) gun[8], a superconducting RF gun[9] and a direct current (DC) gun[7]. There also exist proposals with combinations of these methods, called hybrid configurations[3].

1.2.1 Very high frequency guns

A very high frequency gun is a normal conducting RF photo-gun that operates using RF frequencies in the very high frequency range from 30 to 300 MHz. RF photo-guns produce electron bunches by shooting a short laser pulse on a cathode material, after which electrons are emitted at the surface and accelerated by the RF electric field. The required photon energy to release electrons from the surface is high; the energy of a photon needs to be higher than the work function of the cathode material. Yttrium, for example, has a work function of about 3.1 eV, which closely matches the photon energy of commercially available frequency doubled Ti:Sapphire lasers[10]. The normal conducting RF technology that is currently used operates at RF frequencies of 1 to 3 GHz and the frequency of the electron bunches released, the repetition rate, of the electron sources using this technology is typically limited to kHz. This concept cannot be up-scaled to repetition rates higher than around 10 kHz due to the excessive power dissipated on the RF cavity walls inside the gun in order to maintain the required accelerating fields when operating in continuous wave (CW) mode. Operating at MHz frequencies (up to 700 MHz) lowers the power that is dissipated on the cavity walls to an acceptable level that can be cooled using water cooling while operating in CW mode. When operating in the VHF range from 30 to 300 MHz, the dissipated power is not an issue anymore. Another benefit of the lower (30-300 MHz) frequency range is that the longer wavelengths allow for simpler cavity designs with bigger apertures at the exit of the cavity without causing significant perturbations to the RF fields. The CW operation is combined with a complex laser system operating at higher

frequencies, higher harmonic generation to reach larger photon energies and special semiconductor cathode materials with a low work function to reach MHz repetition rates. Semiconductor cathodes, such as Cs2Te or multi-alkali antimonides, offer very high initial quantum efficiencies (QE) of 10^{-1}, but they are very delicate and reactive and would need to be replaced weekly due to a decrease in their quantum efficiency. Operating such cathodes with these quantum efficiency lifetimes requires an ultra-high vacuum pressure lower than 10^{-10} mbar. The Lawrence Berkeley National Laboratory (LBNL) has developed a VHF gun operating at 186 MHz to be used as the electron source for the Linear Coherent Light Source-II (LCLS-II). The gun, called APEX, operates at a voltage of 750 kV with a cathode gradient of 20 MV/m in phase-II. It is about 4 meters long. For the normal conducting continuous wave RF electron guns, repetition rates higher than 700 MHz are beyond their capabilities.

1.2.2 Superconducting RF guns

Superconducting RF guns are capable of reaching repetition rates of GHz and higher. They continue where the above mentioned normal conducting RF guns are limited by eliminating the Ohmic limitations on the walls of the RF cavity. The compatibility with the high quantum efficiency semiconductor cathodes is, however, more limited due to the cryogenic temperatures and external magnetic fields cannot be applied[3]. A research group at Helmholtz Zentrum Dresden Rossendorf (HZDR) has developed such an SRF gun and its second iteration is capable of delivering 200 pC pulses sub-ps in length with a 100 kHz repetition rate[11]. The downside of superconducting RF guns are the superconducting cooling requirements and the more expensive components.

1.2.3 Direct current guns

The repetition rate of RF guns is dependent on the RF frequency that is used, whereas the repetition rate of DC gun schemes are not limited by the RF frequencies as there is a static (or pulsed) electric field applied always pointing in the same direction. The guns can be operated with magnetic fields in the cathode area and are compatible with all cathode materials currently available. When a DC electric field is applied, the electrons can be extracted in two ways: through photo-emission and thermionic emission. Photo-emission has been described in section 1.2.1 and there currently is a DC photo-emission electron gun operational, a setup at Cornell University in the US, that is capable of reaching a repetition rate in the GHz range[12]. It creates bunches with a charge of 77 pC and an emittance of 0.72 mm mrad at a repetition rate of 1.3 GHz. It is complex and expensive to operate however. The areas where DC guns still need improvement are in increasing the beam energies and increasing the electric field gradients at the cathode.

Thermionic emission is a thermally induced emission of electrons from a surface. By heating the cathode the thermal energy of the electrons can overcome the work function, after which the electrons at the surface can leave the material. This process is described in more detail in section 2.1 of this report. Thermionic cathode materials with very low work functions, such as LaB_6 and CeB_6, can provide current densities up to 20 A/cm^2. For example, a 500 kV pulsed DC thermionic electron gun using a CeB6 cathode has been developed by researchers at SACLA to be used as an injector for the x-ray FEL at the SPring-8 facility[13].

1.3 DC Thermionic gun

Considering the operating requirements and costs, we have chosen to pursue the DC thermionic electron emitter pathway with a 100 kV thermionic gun in combination with RF cavities capable of operating at a repetition rate of 1.5 GHz. Using thermionic emission greatly reduces the constraints

on the system. The required vacuum is *only* around 10^{-6} mbar and, depending on the pressure, the lifetime of the cathode can be up to several thousand hours, which in operational setting means multiple years. The drawback is that the emission current is continuous, while RF accelerator structures require nicely spaced bunches of electrons. Using chopper and compressor RF cavities, the continuous current can be transformed into a train of bunches exiting the gun. An illustration of this concept is shown in figure 1.1, which shows the continuous current from the emitter being chopped after the first RF cavity and compressed in the second cavity. This will, however, result in a loss of total output current compared to the initial emission current. The idea for this electron gun is to use multiple harmonics inside both cavities to achieve a 30% duty cycle. More on this can be found in section 2.4.

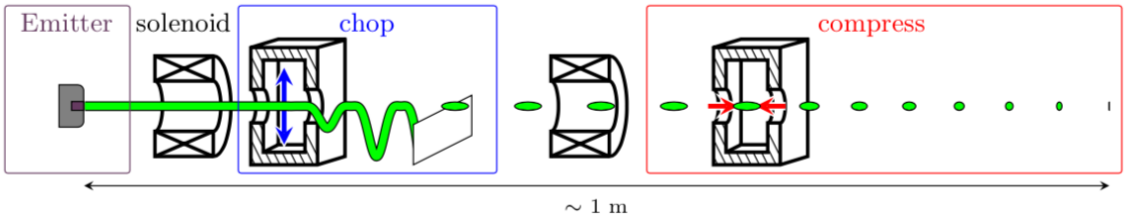

Figure 1.1: The DC thermionic gun setup to achieve a bunched output[7]. A continuous beam of electrons starts at the emitter on the left. It then goes through the solenoid into the chopper RF cavity, which operates using multiple magnetic fields. The knife-edge cuts off the deflected part of the beam. The leftover particles continue in the direction of propagation and enter the compressor RF cavity, after which the compression point is shown at the last electron bunch at the end.

1.4 Emitter temperature

The gun has been designed with the goal of keeping the emittance low, while maintaining a high average beam current. The best way to do this is to keep the electron emitter surface small and operate it a high temperature. The reasoning behind this is described in section 2.2. The temperature cannot be increased indefinitely, however. If the emitter reaches temperatures above 1800K, the structure of the emitter holder will start to lose its structural strength and can tip over making the emitter unusable. On top of this, higher temperatures will increase the current density, which also has its limit. This limit is given by the Child-Langmuir law, which describes how the space charge of the emitted electrons will counteract the electric field of the accelerating structure. Section 2.1.1 describes this effect in more detail. To carefully find the optimal operating temperature, without harming the emitter, the temperature should be accurately monitored and controlled.

1.4.1 Dual wavelength pyrometry

There are many ways to measure temperatures, ranging from mercury glass thermometers to Langmuir probes (for electron temperatures in plasmas). All methods boil down to two main different forms of measuring; directly or indirectly, or also known as invasive and non-invasive methods. The absolute or relative change in the properties of the heated material can be monitored. This is often difficult, because usually the measured object does not have well defined dimensions, varying material purity or other unknown properties. Therefore it is easier to place a known object or material in thermal equilibrium with the target object. As it equilibrates with the object of interest, the temperature of both objects can be determined based on the measured change of a known property.

The emitter in the experimental setup has a diameter of 300 µm, on which a negative potential of -100 kV is applied. These experimental constraints make it difficult to get close to the emitter, let alone

be in contact with it. The temperature is therefore monitored by looking at the black body radiation that is emitted by the electron emitter, as this is a property only depending on the temperature and the emissivity of the object. The emissivity is a measure for the ability of the surface to emit energy in the form of light. Instead of capturing the complete black body spectrum, the intensity of the emitted black body radiation is measured for one or multiple bands of wavelengths. The temperature can be calculated using the intensity of the radiated light or the ratio of the intensities of the specific wavelengths. The focus of this report will be on using the ratio with a technique that known as dual wavelength pyrometry and is described in section 2.3.6.

Chapter 2

Theory

This chapter starts with the explanation of the theory behind thermionic emission in section 2.1. The temperature measurement will be explained in section 2.3, including black body radiation in section 2.3.3, and different methods in sections 2.3.5, 2.3.6, 2.3.7 and 2.3.8. The RF cavities are described in section 2.4 and the imaging using lenses in section 2.5.

2.1 Thermionic emission

The thermally induced emission of charge carriers from a surface is called thermionic emission. The charge carriers, usually electrons, leave the surface when the thermal energy given to them surpasses the work function of the material. The work function refers to the minimum amount of energy needed for an electron to leave the material without being pulled back in. It is a characteristic property of the surface of a material and, for metals, it is typically in the order of electron volts. As the electrons leave the surface, they leave behind an equal charge with opposite sign in the emitting area. The emitter is typically connected to a power source to replenish the charge that has left the material through emission and neutralize the emitter. For metals in vacuum, thermionic emission becomes considerable at temperatures of 1000 K and higher[14].

Thermionic emission is described by the Richardson-Dushman equation[15]:

$$J = A_g T^2 \mathrm{e}^{\frac{-W}{k_\mathrm{b} T}}, \tag{2.1}$$

in which J is the current density emitted by a thermionic emitter, A_g the Richardson constant, T the temperature of the emitter, k_b the Boltzmann constant and W the work function of the material. Experimentally it has been found that the Rchardson constant A_g is material dependent[16]. Therefore A_g is defined as a universal constant A_0 multiplied by a material specific correction factor b:

$$A_g = b \cdot A_0, \tag{2.2}$$

in which the universal constant A_0 is given by

$$A_0 = \frac{4\pi m_e {k_b}^2 e}{h^3}, \tag{2.3}$$

where m_e is the mass of an electron, e the charge of an electron and h is Planck's constant. The

numerical value of A_0 comes out to be $1.20173 \times 10^6 \mathrm{Am}^{-2}\mathrm{K}^{-2}$. An overview of the values of A_g and W for different materials is given in section 2.1.3.

From equation 2.1 it can be seen that the emission current J scales with $T^2 \mathrm{e}^{\frac{1}{T}}$. This relationship is shown in figure 2.1, in which the emission current has been plotted as a function of temperature for LaB_6 and tantalum, two materials that are used as emitters, with values of 29 $\mathrm{Acm}^{-2}\mathrm{K}^{-2}$ and 60 $\mathrm{Acm}^{-2}\mathrm{K}^{-2}$ for A_g and 2.7 eV and 4.12 eV for W for LaB_6 and tantalum respectively. The emission current of the two materials differs by several orders of magnitude. This is due to the material properties, i.e. different work functions and material specific correction factors. The increase of the temperature does have a similar effect on the emission current of both materials.

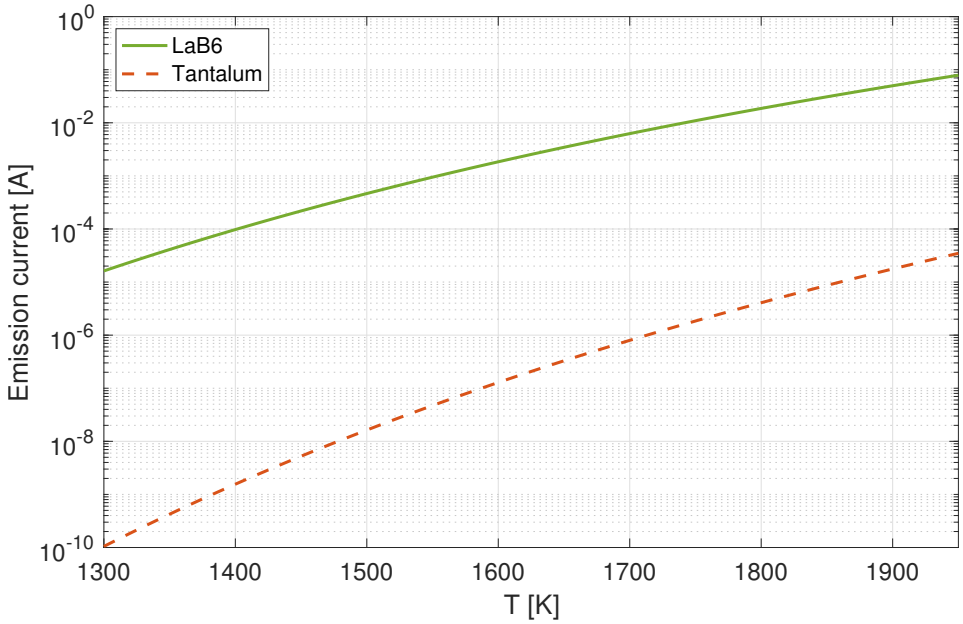

Figure 2.1: The emission current for LaB_6 (solid line) and Tantalum (dashed line) as is calculated using the Richardson-Dushman equation, equation 2.1, using values of 29 $\mathrm{Acm}^{-2}\mathrm{K}^{-2}$ and 60 $\mathrm{Acm}^{-2}\mathrm{K}^{-2}$ for A_g and 2.7 eV and 4.12 eV for W for LaB_6 and tantalum respectively.

2.1.1 Schottky effect

Typically, a voltage will be applied to electron emission devices to create an electric field at the surface of the emitter. The electric field is used to accelerate electrons away from the emitter, as is done in electron guns, but it also increases the emission current by lowering the surface barrier. The latter is called the Schottky effect and also known as field enhanced thermionic emission or Schottky emission. When there is no electric field, as is described by equation 2.1, the escaping Fermi-level electrons encounter a barrier with height W equal to the work function of the material. If there is an electric field present, it lowers this barrier seen by the escaping electrons by ΔW, which increases the emission current in comparison to ordinary thermionic emission[16]. This is shown in figure 2.2. ΔW, by which the barrier is lowered, is given by

$$\Delta W = \sqrt{\frac{e^3 E}{4\pi\varepsilon_0}}, \tag{2.4}$$

with E being the electric field strength and ε_0 the vacuum permittivity. Incorporating this into the

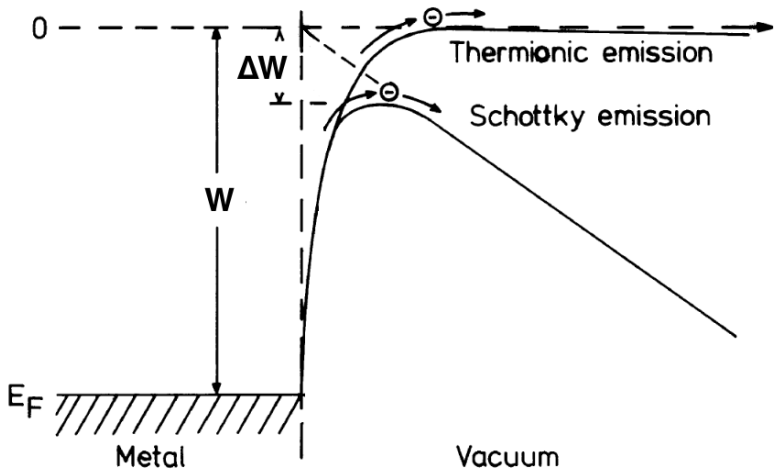

Figure 2.2: An energy level diagram of a metal, in which the energy barriers for Schottky emission and thermionic emission are compared. W represents the work function of the metal. Adapted from [18].

original thermionic emission equation 2.1, the expression becomes

$$J = A_g T^2 \exp\left(\frac{-(W - \Delta W)}{k_b T}\right). \tag{2.5}$$

Field enhanced thermionic emission described by this equation is accurate for electric field strengths up to about 10^8 Vm^{-1}. For higher electric field strengths, quantum effects such as Fowler-Nordheim tunneling start to contribute to the electron emission current and can even dominate when operating in the cold field electron emission regime[17].

The current density cannot be increased indefinitely. The current density limit is determined by the Child-Langmuir law. This law states that at the current density limit, the space charge created by the freed electrons generates an electric field at the surface of the emitter equal in magnitude to that of the accelerating DC electric field in opposite direction. The electric fields will counteract each other and current densities close to the limit will therefore result in a small net electric field. This will only slowly accelerate the escaping electrons, which gives space-charge effects more time to affect the beam with a significant increase in transverse emittance. To preserve a low emittance, operation in this regime should be avoided. For an infinite emitter area emitting electrons towards an infinitely long parallel plate the Child-Langmuir law is theoretically determined to be[19]

$$J_{\max} = \frac{4\varepsilon_0}{9}\sqrt{\frac{2e}{m_e}}\frac{V_0^{3/2}}{d^2}, \tag{2.6}$$

with V_0 and d being the potential difference and the distance between the parallel plate electrode respectively. The law assumes no scattering of the electrons in between the electrodes and that the electrons have a zero velocity at the cathode surface. In reality however, the Child-Langmuir limit is higher and should be multiplied by a correction factor based on the ratio of the radius of the emitter surface to the distance between emitter and the anode[7].

2.1.2 Emittance

When the extracted electrons leave the surface, the beam will start to diverge. The end goal in this experiment is to inject the extracted electrons into an RF accelerator-based light source. This means that the divergence of the beam and the energy spread of the electrons in the beam should be kept small enough to enter the accelerator. The specific requirements depend on the application. Beam quality is therefore a crucial aspect of the electron gun. The beam quality is represented by the transverse normalized root mean square (rms) emittance, given by

$$\varepsilon_{\mathrm{n,rms}} = \gamma\beta\sqrt{\langle x^2\rangle \langle x'^2\rangle - \langle xx'\rangle^2}, \tag{2.7}$$

in which γ is the Lorentz factor, β the velocity of an object relative to the speed of light, x the transverse position and $x\prime$ the divergence. In the paraxial approximation, the divergence $x\prime \approx v_x/v_z$. However, at the surface of the electron emitter, the electrons have not gained enough speed yet for this approximation to be valid. For a circular thermionic emitter with a flat surface the initial emittance is given as the thermal emittance $\varepsilon^{\mathrm{th}}_{\mathrm{n,rms}}$, which is calculated as

$$\varepsilon^{\mathrm{th}}_{\mathrm{n,rms}} = \frac{r}{2}\sqrt{\frac{k_b T}{m_e c^2}}, \tag{2.8}$$

in which c is the speed of light and r the radius of the circular emitter surface.

2.1.3 Electron emitters

For thermionic emission thermionic electron emitters are needed. These are made using materials that release electrons when heated to a sufficient temperature. Generally materials are used that have low work functions and high melting points in order to maximize the current that can be generated, without the material itself getting damaged. Table 2.1 shows an overview of the important emission properties for lanthanum hexaboride (LaB_6), cerium hexaboride (CeB_6), Tantalum (Ta) and Tungsten (W). LaB_6 is able to reach the highest thermionic emission current density and has therefore been chosen as thermionic electron emitter. There still are some unknown effects of surface contamination and corrosion during operation and for this reason CeB_6 is chosen as an alternative. Despite having a lower thermionic emission current density compared to LaB_6[20], CeB_6 is supposed to be more corrosion resistant. This will still have to be verified experimentally, but that is why both are included. Tantalum is used to test the experimental setup, as it is a cheaper alternative to LaB_6. The thermionic emission current density is orders of magnitude lower than LaB_6 (see figure 2.1), but this is not relevant for the purpose of its testing use. Tungsten is added for comparison.

Table 2.1: Properties of different materials that can be used as thermionic electron emitters.

Property	LaB_6	CeB_6	Ta	W
Work function [eV]	2.7	2.65	4.12	4.54
A_g [$Acm^{-2}K^{-2}$]	29	3.6	60	60
Melting point [K]	2483	2463	3290	3695
Typical operational temperature [K]	1800	1800	2200	2600

Lanthanum hexaboride

LaB_6 is an inorganic chemical that is widely used in small spotsize, for e.g. electron microscopes, and high electron current applications. The low work function enables higher currents at lower temperatures of the cathode. LaB_6 has one of the highest electron emissivities known and is stable in vacuum. Compared to tungsten, hexaboride cathodes are about 10 times brighter, meaning a higher number of electrons per unit area, and have a 50 times longer lifetime[21]. This results in a higher beam current using a smaller surface and less frequent cathode replacement during operation. LaB_6 already starts slowly evaporating from its surface well before it reaches its melting point of 2483 K[21][22]. This is why the operating temperature (in combination with the vacuum pressure) will have an effect on the lifetime on the emitter. An image of the material is shown in figure 2.3.

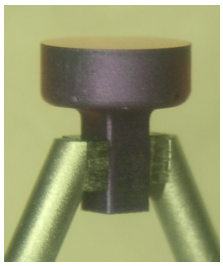

Figure 2.3: An image of lanthanum hexaboride in the form of a so-called tophat emitter shape[23].

Tantalum

Tantalum is a transition metal with a high melting point and a low vapor pressure at high temperatures. It is a great cheap general purpose thermionic emitter. At room temperature it is chemically inert and therefore highly corrosion resistant, but at temperatures above 700 K it starts oxidizing in the presence of water vapor and above 1200 K tantalum nitrides form when there is nitrogen present. The emitting characteristics will degrade when these compounds form at the surface.

2.2 Emission current

Using the current density from equation 2.5 we can calculate the electron current coming off the emitter by multiplying it by the area of the circular emitter πr^2. The emission current then becomes:

$$I = \pi r^2 A_g T^2 \exp\left(\frac{-(W - \Delta W)}{k_b T}\right). \tag{2.9}$$

From this equation and equation 2.8 it becomes evident that the emission current of the electron emitter I scales with r^2 and $T^2 e^{\frac{1}{T}}$, while the emittance $\varepsilon^{\text{th}}_{\text{n,rms}}$ of beam scales with with r and $\sqrt{T}$. Figure 2.4 shows how the emission current and the thermal emittance of the beam depend on the temperature with an emitter diameter of 300 μm.

As the goal of the gun in this experiment is to create a high current beam with the lowest possible emittance, it is preferable to keep the radius of the emitter small, while maximizing the temperature of the crystal. This way the emittance is minimized at any desired beam current. Lanthanum hexaboride melts at 2483 K, but the upper limit is determined by the supporting structure around it, which is necessary for the experiment. At temperatures above 1800 K the structural strength of

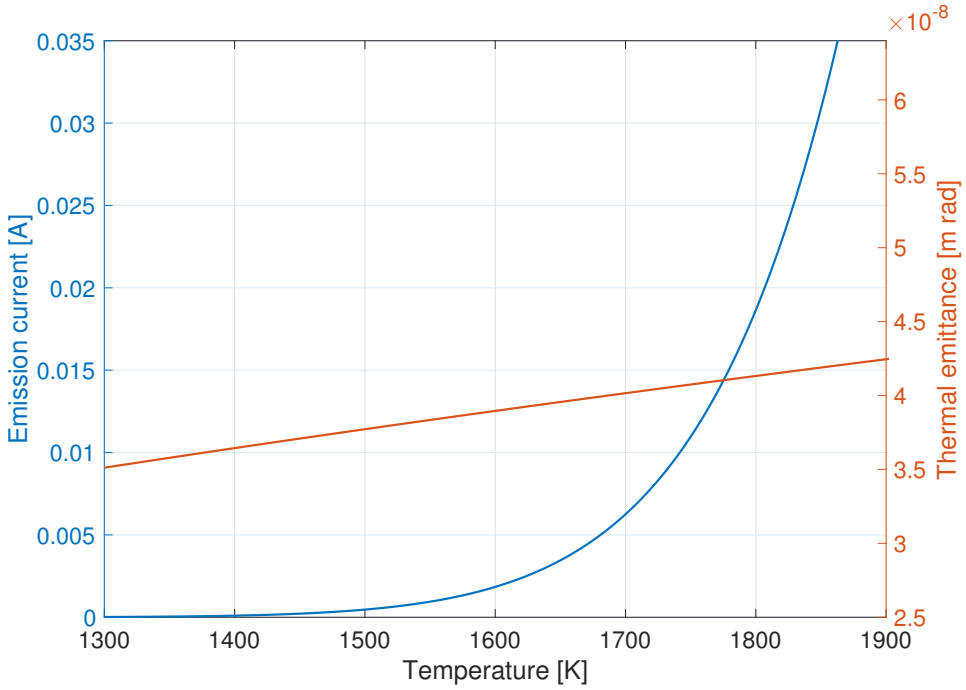

Figure 2.4: The thermionic emission current and the thermal emittance as a function of temperature for the LaB_6 emitter with a diameter of 300 µm.

the support structure becomes too low, thus making it unstable. When it bends or breaks it cannot be repaired and the support structure with the emitter has to be replaced. The goal is therefore to operate close to 1800 K, but not go over it. Temperature control is an important part of the setup.

2.3 Temperature measurement

There are many ways of measuring the temperature of an object. Most methods work by measuring a physical property of a material that is known to vary with temperature. There are essentially two categories of temperature measurements: Contact and non-contact methods, also called invasive and noninvasive[24]. The requirement of the design of the thermionic gun in this project is an absolute temperature measurement in the temperature range of 1000 K to 1800 K with an error margin of 2.27 %.

2.3.1 Choice of method

As a material heats up, its properties change. Different properties of different materials can be used to determine a temperature. Thermocouples are often used, utilizing two dissimilar electrically conducting wires forming electrical junctions at differing temperatures based on the thermoelectric effect. This creates a temperature dependent voltage that can be calibrated to the correct temperature. Another property that changes with temperature is the resistance of a material. Thermistors are resistors, of which the resistance depends of the temperature, more so than normal resistors. These methods can be very precise, but are relatively slow, depending on the heat transfer properties of the system.

By introducing another object and bringing it in thermal equilibrium with the object of interest, it takes away or adds heat to the system to reach the point of thermal equilibrium. This means it perturbs the system of interest. To avoid this, several non-invasive thermometric techniques have

been developed. There are again two distinct ways of approaching this. One way is to look at the electromagnetic radiation that the object is emitting and the second approach involves sending an signal, usually electromagnetic or sound waves, in order to look for resonances or to activate another process.

Starting with the latter, you can think of laser induced fluorescence (LIF), Coherent anti-Stokes Raman spectroscopy (CARS), or laser absorption spectroscopy. Many of them have been developed for medical or biological applications, but also for engines, gas-turbines, and synthesis reactors. The capabilities of such optical-based techniques enable very fast measurements with timescales down to nanoseconds[25].

Looking only at the electromagnetic radiation coming from the object of interest, the temperature of the surface can be determined based on the amount of thermal radiation emitted by the object at its surface. This process is known as pyrometry.

2.3.2 Pyrometry

There are different pyrometry methods, each with their own pyrometer equipment. A digital pyrometer consists of optics, to focus the light, and a detector, onto which the light is focused. The detector generates an output signal related to the radiant emittance $j^\star$ in W/m^2 of the target object, which scales with T^4 as is stated by the Stefan-Boltzmann law[26]:

$$j^\star = \varepsilon \sigma T^4, \tag{2.10}$$

in which ε is the emissivity and σ the Stefan-Boltzmann constant. Optical pyrometers exist also, but here the operator looks through a mini telescope and has to make a manual measurement. Digital pyrometers use two types of detectors: photo-diodes that generate a current based on the number of incident photons and thermopiles that generate a potential difference across the detector based on the absorbed energy of the incoming photons[27].

Some pyrometers measure the complete spectrum of the emitted radiation, usually done using thermopiles, and are therefore called wideband pyrometers. It is, however, not necessary to capture the entire spectrum to determine the temperature. Narrow-band pyrometers capture a smaller and more specific part of the spectrum. Which part of the spectrum depends on the application for which it will be used. While most pyrometers use a single band to determine the temperature, the accuracy can be improved by combining multiple bands from the spectrum. These pyrometers usually use 2 separate bands and, in that case, are called ratio or dual-wavelength pyrometers. The ratio of the two intensities is then related to the temperature of the object.

Experimental restrictions can make it difficult to bring another object close to and in thermal equilibrium with the emitter, so contact methods are difficult to implement. The restrictions in this experiment include a small emitter with a size of only 300 µm in diameter and a voltage of -100 kV will be applied to it during operation (more on this in section 3). Furthermore, the budget does not allow for a spectrometer to capture a wide infrared spectrum. Therefore 4 different pyrometry methods will be introduced that can be used for the temperature measurement, with the focus on dual wavelength pyrometry. Section 2.3.5 will explain single band pyrometry, section 2.3.6 will explain dual wavelength pyrometry, section 2.3.7 will introduce a calibration method to increase the accuracy of the dual wavelength pyrometry method and section 2.3.8 will explain the use of a CCD chip. First, section 2.3.3 will give a more detailed overview of black body radiation.

2.3.3 Black body radiation

All ordinary matter emits electromagnetic radiation. In order to stay in thermal equilibrium, it must emit electromagnetic radiation at an equal rate or lower as it absorbs it. Equation 2.10 showed that the total radiance of the thermal radiation emitted from an object scales with T^4, but if we take a closer look, it becomes evident that also the spectrum itself has a characteristic shape. This is called the black body spectrum. A black body is an ideal object that absorbs all electromagnetic radiation that strikes its surface, hence it is called a black body. This characteristic radiation has a specific spectrum and intensity that (ideally) only depends on the temperature of the object. The spectral radiance emitted by a black body in thermal equilibrium at temperature T, is quantitatively embodied in Planck's law[28]:

$$E(\lambda, T) = \frac{2hc^2}{\lambda^5} \frac{1}{e^{\frac{hc}{\lambda k_b T}} - 1} = \frac{C_1}{\lambda^5} \left(e^{C_2/\lambda T} - 1 \right)^{-1}, \tag{2.11}$$

where λ is the wavelength and C_1 and C_2 are constants defined as $2hc^2$ and hc/k_b respectively. Figure 2.5 shows the black body spectrum for three different temperatures. It can be seen that the intensity of the total radiation, meaning the integral over all wavelengths, increases significantly as the temperature increases as was described in equation 2.10. Furthermore, the peak of the black body spectrum shifts to the left as the temperature increases.

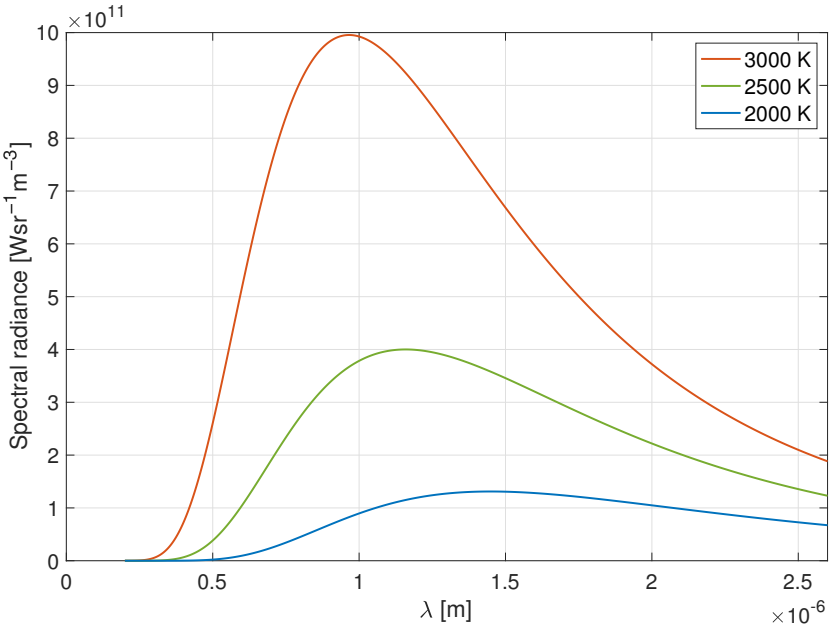

Figure 2.5: Theoretical spectrum of black body radiation for 2000 K, 2500 K and 3000 K.

For short wavelengths, i.e. $\lambda \ll C_2/T$, and temperature below 2000 K, the Planck function in equation 2.11 can be replaced by the Wien approximation:

$$\left(e^{C_2/\lambda T} - 1 \right)^{-1} \approx e^{-C_2/\lambda T}. \tag{2.12}$$

Substituting this in Plancks law, equation 2.11 then becomes

$$E(\lambda, T) = \frac{C_1}{\lambda^5} e^{-C_2/\lambda T}. \tag{2.13}$$

For a wavelength of 1050 nm the difference between the calculated spectral radiance from equation 2.11 and 2.13 is 0.04 % at 1760 K.

Real materials only emit energy at a fraction of the energy of the black body radiation as defined in equation 2.11. This fraction is called the emissivity ε of an object and ranges from 0 to 1, with 0 meaning no radiation and 1 meaning perfect black body radiation. An object with an emissivity smaller than 1 and independent of the frequency of the emitted radiation is called a gray body[29]. Most materials however, have a non constant emissivity varying with the frequency of the emitted radiation and the temperature of the object. These three scenarios are visualised in figure 2.6 with arbitrarily chosen emissivity values.

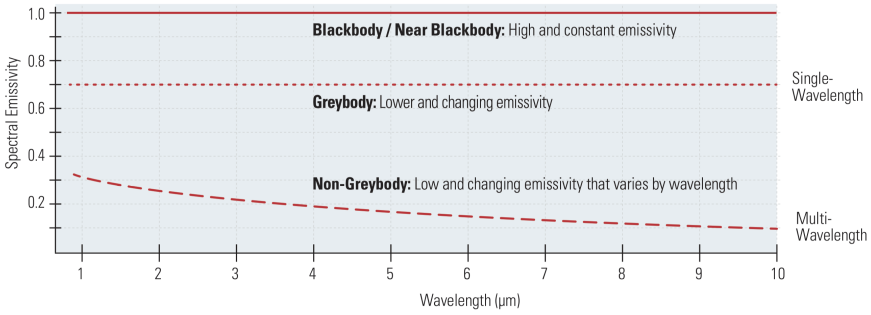

Figure 2.6: An illustration of the different emissivity scenarios and what type of pyrometry is preferred. Adopted from [30].

To account for the non-ideal emitted radiation, an additional term for the emissivity $\varepsilon(\lambda)$ as a function of the wavelength, is added to equation 2.13, which results in

$$E(\lambda, T) = \varepsilon(\lambda) \frac{C_1}{\lambda^5} e^{-C_2/\lambda T}. \tag{2.14}$$

2.3.4 Detectors

The black body radiation can be captured using different detectors. For these experiments photodetectors based on photodiodes and a CCD camera are used. A CCD (charge-coupled device) camera contains an image sensor with an array of pixels that are represented by metal-oxide-semiconductor (MOS) capacitors. During image acquisition the photons are converted into electric charges at the semiconductor-oxide interface. CCDs can move the charges between the capacitive bins and read out these charges. Photodiodes on the other hand, are semiconductor devices that convert photons into an electrical current.

Reverse bias

An ordinary photodiode generates a current without the need of an external power supply. This operational mode is called photovoltaic. To improve frequency response and the linearity of the signal, the photodiode can be operated in photoconductive mode. By applying an external reverse bias the width of the depletion zone of the p-n junction increases. This increases responsivity by decreasing the junction capacitance and produces a linear response proportional to the input optical

power. It does also tend to increase dark current, but in this case a linear response is more important. The responsivity R of the photodiode is then given by the ratio of the generated photocurrent I_{PD} to the light power P falling onto the photodiode at a given wavelength[31]:

$$R(\lambda) = \frac{I_{PD}}{P}. \tag{2.15}$$

This relationship is important, because it allows us to interpret the increase of the current signal I directly proportional to the increase of the light power at the specific wavelengths. There is, however, no information on the error of the linear response behavior of the detectors.

2.3.5 Single band pyrometry

A range of wavelengths single band pyrometry a single band of wavelengths is used to determine the shape of the black body spectrum and the corresponding temperature. The spectral radiance emitted by a source can be measured using a photodetector. A typical setup is shown figure 2.7. It includes a source and a lens to focus the radiated light on the photodetector.

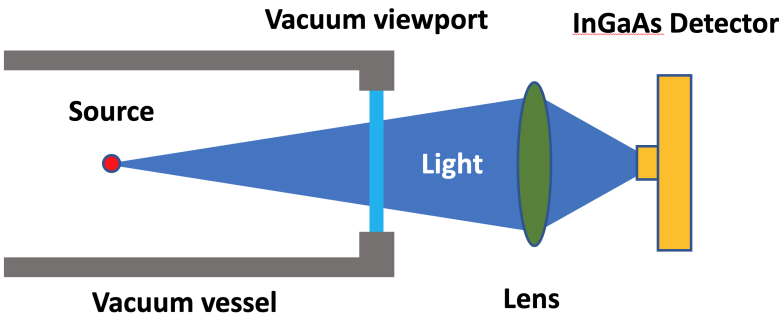

Figure 2.7: A typical setup to measure the spectral radiance of a light source, which includes a source, a viewport, a lens and a detector.

The measured signal is the current from the photodetector. From equation 2.3.4 it is known that the current I scales with the power P of the light reaching the detector as

$$I = R(\lambda) \cdot P. \tag{2.16}$$

P can be calculated from the radiance $L(\lambda, T)$ when taking into consideration the solid angle Ω and the radiating area A_{source} of the light source through:

$$P = \Omega \cdot A_{\text{source}} \cdot L(T), \tag{2.17}$$

in which $L(T)$ is the radiance defined as $\mathrm{Wm^{-2}sr^{-1}}$. The radiance can be calculated from the spectral radiance through

$$L(T) = \int_0^\infty E(\lambda, T) \cdot \mathrm{d}\lambda. \tag{2.18}$$

Using equation 2.16, 2.17 and 2.18, I can be calculated as a function of temperature as

$$I(T) = \Omega A_{\text{source}} \int_0^\infty E(\lambda, T)\tau(\lambda)R(\lambda) \cdot \mathrm{d}\lambda, \tag{2.19}$$

in which $\tau(\lambda)$ is included to account for the optical losses of the optical components in the setup. In case of figure 2.7 losses are due to the transmission spectrum of the lens. Using equation 2.14, equation 2.19 can be written as

$$I(T) = \Omega A_{\text{source}} C_1 \int_0^\infty \frac{\varepsilon(\lambda)\tau(\lambda)R(\lambda)}{\lambda^5} e^{-C_2/\lambda T} \cdot \mathrm{d}\lambda. \tag{2.20}$$

When the dimensions of the setup, the emissivity $\varepsilon(\lambda)$ and the detector sensitivity $R(\lambda)$ are known, the current I can be predicted for a range of temperatures using equation 2.20.

Uncertainty

This method is commonly used in commercially available pyrometers and its uncertainty ranges from around 1 % to 10 % or more. It mainly depends on how accurately the emissivity of the object is known and for objects at larger distances or behind obstructions, the error in the transmission losses and reflections will increase the uncertainty. The standard deviation of the measured signal I is given by:

$$\delta I_{\text{det}} = I_{\text{det}} \sqrt{\left(\frac{\delta\Omega}{\Omega}\right)^2 + \left(\frac{\delta A_{\text{source}}}{A_{\text{source}}}\right)^2 + \left(\frac{\delta\epsilon}{\epsilon}\right)^2 + \left(\frac{\delta\tau}{\tau}\right)^2 + \left(\frac{\delta R}{R}\right)^2}. \tag{2.21}$$

The uncertainty in the current does not scale linearly with the uncertainty of the temperature. The exact error depends on the temperature of interest and the setup, but due to the uncertainty in the emissivity of the emitter surface and an uncalibrated detector responsivity curve across all wavelengths within the range of the detector, the temperature uncertainty is likely in the range of 5 to 10 %. Section 3.7.2 describes the specifics of the setup and the corresponding error. Without calibrated components the setup is very susceptible to systematic errors. Calibration requires the calibration setup to have the same dimensions, meaning the same emitter area in combination with the same solid angle to create the same intensity for a known source.

2.3.6 Dual wavelength pyrometry

Instead of looking at a single band of the spectral radiance, the intensity of two different wavelengths reaching the detector can be compared. Using equation 2.14, the spectral radiance for a specific wavelength λ_1 and its corresponding $\varepsilon_{\lambda 1}$ can be calculated:

$$E_{\lambda 1}(T) = \varepsilon_{\lambda 1} \frac{C_1}{\lambda_1^5} e^{-C_2/\lambda_1 T}. \tag{2.22}$$

The same can be done for λ_2 and its corresponding $\varepsilon_{\lambda 2}$, after which the ratio of the two is given as:

$$\frac{E(\lambda 1, T)}{E(\lambda 2, T} = \frac{\varepsilon_{\lambda 1} \frac{C_1}{\lambda_1^5} e^{-C_2/\lambda_1 T}}{\varepsilon_{\lambda 2} \frac{C_1}{\lambda_2^5} e^{-C_2/\lambda_2 T}}. \tag{2.23}$$

Then, equation 2.23 can be rewritten to create a function for T, given by

$$T = \frac{C_2 \left(\frac{1}{\lambda_2} - \frac{1}{\lambda_1}\right)}{\ln \frac{E(\lambda 1, T)}{E(\lambda 2, T)} - \ln\left(\frac{\varepsilon_{\lambda 1}}{\varepsilon_{\lambda 2}}\right) - 5 \ln\left(\frac{\lambda_2}{\lambda_1}\right)}. \tag{2.24}$$

Figure 2.8 shows a typical dual wavelength setup, in which the beam is split to detect the intensities of the light at two different wavelengths. It consists of multiple lenses, that guide the light through a beamsplitter and two band-pass filters towards two separate detectors.

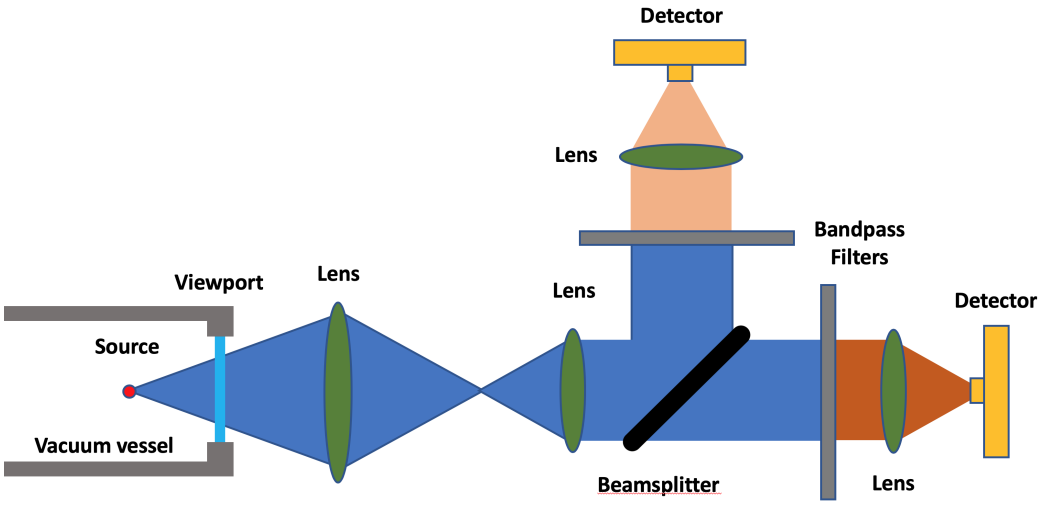

Figure 2.8: A typical setup to measure the radiance of a light source for multiple wavelengths, which includes a source, multiple lenses, a beamsplitter, two band-pass filters and two detectors.

In order to use equation 2.24, the relationship between the ratio of the response signal I of the detectors and the ratio of the radiance E of the source at both wavelengths needs to be known. Equation 2.15 showed that that signal I from the detector is linearly proportional to the power P of the incident light. Thus, when looking at the ratio for two different wavelengths, the dimensions of the setup cancel out through

$$\frac{I_{\lambda 1}(T)}{I_{\lambda 2}(T)} = \frac{R_{\lambda 1} P_{\lambda 1}(T)}{P_{\lambda 2} P_{\lambda 2}(T)} = \frac{R_{\lambda 1} \Omega A_{\text{source}} L_{\lambda 1}(T)}{R_{\lambda 2} \Omega A_{\text{source}} L_{\lambda 2}(T)} = \frac{R_{\lambda 1} L_{\lambda 1}(T)}{R_{\lambda 2} L_{\lambda 2}(T)} \tag{2.25}$$

This is only valid because for the setup described in section 2.8 the solid angle and the source are identical for both wavelengths. The radiance for wavelength λ_1 can be calculated using

$$L_{\lambda 1}(T) = \int_{\lambda_{\text{low}}}^{\lambda_{\text{high}}} E(\lambda, T)\eta(\lambda) \cdot \mathrm{d}\lambda, \tag{2.26}$$

in which $\eta(\lambda)$ is the transmission correction for all optical elements and the integration boundaries λ_{low} and λ_{high} are the bandwidth of the narrow band-pass filter centered around λ_1. In the case of figure 2.8 equation 2.26 becomes

$$L_{\lambda 1}(T) = \int_{\lambda_{\text{low}}}^{\lambda_{\text{high}}} E(\lambda, T) \cdot \tau_{\text{lens}}(\lambda)^3 \cdot \tau_{\text{viewport}}(\lambda) \cdot \tau_{\text{beamsplitter}}(\lambda) \cdot \tau_{\text{filter}}(\lambda) \cdot \mathrm{d}\lambda, \tag{2.27}$$

with the transmission of the lenses $\tau_{\text{lens}}(\lambda)$, the transmission of the band-pass filters $\tau_{\text{filter}}(\lambda)$, the transmission of the dichroic beam splitter $\tau_{\text{beamsplitter}}(\lambda)$ and transmission of the viewport $\tau_{\text{viewport}}(\lambda)$. When the narrow band-pass filter has a small bandwidth with the center at wavelength λ_1 and the transmission values can be assumed constant for the optical components at λ_1 within the bandwidth of the band-pass filter, the integral in equation 2.27 can be simplified to

$$L_{\lambda 1}(T) = E(\lambda_1, T) \cdot \tau_{\text{lens}}(\lambda_1)^3 \cdot \tau_{\text{viewport}}(\lambda_1) \cdot \tau_{\text{beamsplitter}}(\lambda_1) \cdot \sigma_{\text{filter},\lambda 1}, \tag{2.28}$$

with $\sigma_{\text{filter},\lambda 1} = \int_{\lambda_{\text{low}}}^{\lambda_{\text{high}}} \tau_{\text{filter},\lambda_1} \mathrm{d}\lambda$. The same can be done for λ_2, but for λ_2 instead of the transmission spectrum of the beamsplitter the reflection spectrum is used and a different narrow band-pass filter, corresponding to the wavelength, is used. Then looking again at the ratio $\frac{I_{\lambda 1}(T)}{I_{\lambda 2}(T)}$ for the wavelengths λ_1 and λ_2, using equation 2.28 it then becomes

$$\frac{I_{\lambda 1}(T)}{I_{\lambda 2}(T)} = \frac{R_{\lambda 1} L_{\lambda 1}(T)}{R_{\lambda 2} L_{\lambda 2}(T)} = \frac{R_{\lambda 1} E(\lambda_1, T) \cdot \tau_{\text{lens}}(\lambda_1)^3 \cdot \tau_{\text{viewport}}(\lambda_1) \cdot \tau_{\text{beamsplitter}}(\lambda_1) \cdot \sigma_{\text{filter},\lambda 1}}{R_{\lambda 2} E(\lambda_2, T) \cdot \tau_{\text{lens}}(\lambda_2)^3 \cdot \tau_{\text{viewport}}(\lambda_2) \cdot \tau_{\text{beamsplitter}}(\lambda_2) \cdot \sigma_{\text{filter},\lambda 2}}. \tag{2.29}$$

Thus the ratio $\frac{E(\lambda 1, T)}{E(\lambda 2, T)}$ can be written as

$$\frac{E(\lambda 1, T)}{E(\lambda 2, T)} = F \cdot \frac{I_{\lambda 1}(T)}{I_{\lambda 2}(T)}, \tag{2.30}$$

with F being the correction factor that corrects for the transmission values that are setup specific. In this example for figure 2.8, F is given as

$$F = \frac{R_{\lambda 2} \cdot \tau_{\text{lens}}(\lambda_2)^3 \cdot \tau_{\text{viewport}}(\lambda_2) \cdot \tau_{\text{beamsplitter}}(\lambda_2) \cdot \sigma_{\text{filter},\lambda 2}}{R_{\lambda 1} \cdot \tau_{\text{lens}}(\lambda_1)^3 \cdot \tau_{\text{viewport}}(\lambda_1) \cdot \tau_{\text{beamsplitter}}(\lambda_1) \cdot \sigma_{\text{filter},\lambda 1}}. \tag{2.31}$$

Equation 2.30 can be substituted into equation 2.24 to get T as a function of the ratio of both detector signals. This results in

$$T = \frac{C_2\left(\frac{1}{\lambda_2} - \frac{1}{\lambda_1}\right)}{\ln\frac{I_{\lambda1}(T)}{I_{\lambda2}(T)} + \ln F - \ln\left(\frac{\varepsilon_{\lambda1}}{\varepsilon_{\lambda2}}\right) - 5\ln\left(\frac{\lambda_2}{\lambda_1}\right)}. \tag{2.32}$$

Uncertainty

The current that is measured in the detectors is influenced by similar errors as were described in section 2.3.5, but the uncertainty due to the solid angle and the emitting area do not influence the temperature measurement anymore. However, the increased complexity of the optical setup contributes to more sources of error. The standard deviation in the current signal is now given by

$$\delta I_{\text{det}} = I_{\text{det}}\sqrt{\left(\frac{\delta\epsilon}{\epsilon}\right)^2 + 3\left(\frac{\delta\tau_{lens}}{\tau_{lens}}\right)^2 + \left(\frac{\delta\tau_{bs}}{\tau_{bs}}\right)^2 + \left(\frac{\delta\tau_{vp}}{\tau_{vp}}\right)^2 + \left(\frac{\delta\tau_{filter}}{\tau_{filter}}\right)^2 + \left(\frac{\delta R}{R}\right)^2}, \tag{2.33}$$

with τ_{bs} being the transmission of the beamsplitter and τ_{vp} being the transmission of the viewport.

The key assumption here if systematic errors in the components will result in similar errors for both wavelengths. In other words, if the transmission spectrum of the lens deviates from the suppliers reference spectrum by -2 %, it would likely cause this error to be present at both wavelengths. This means that even though if the error of the measured current in one detector would be 5 %, then the ratio of the two signals results in an error smaller than 5 % and thus making it less sensitive to systematic errors. Therefore a dual wavelength pyrometry setup could be more accurate than a single wavelength pyrometry setup depending on the application. Section 3.4.3 describes the error for the used components.

2.3.7 Reference source

The other way to determine the correction factor F, which we will call F_{ref}, is to use a reference light source with a known temperature, essentially calibrating the setup. Knowing T_{ref}, the known temperature of the reference source, and the detected signals $L_{\lambda1}$ and $L_{\lambda2}$, F_{ref} can be calculated as follows:

$$F = F_{\text{ref}} = \frac{I_{\lambda2}}{I_{\lambda1}}\left(\frac{\lambda_2}{\lambda_1}\right)^5 e^{\frac{C_2\left(\frac{1}{\lambda_2} - \frac{1}{\lambda_1}\right)}{T_{\text{ref}}}}. \tag{2.34}$$

A calibration setup would be similar to the setup described in figure 2.8, but then with a source that has a known reference temperature. The main disadvantage of this method however, is that the reference temperature has to be within the range of temperatures you would like to measure, because for most materials the emissivities will change for different temperatures. Therefore the accuracy of the measurement depends on the accuracy of the temperature of the reference source in the desired range. When the surfaces of the materials are not the same, the different emissivity values of the to be measured source and the reference source also need to be accounted for.

Uncertainty

When calibrated, the uncertainty of the temperature measurement depends mostly on how accurately the temperature of the reference source is known. This is because the transmission curves of all optical components and the sensitivity spectrum of the detector are all calibrated in the calibration. In the

case of using a thermocouple with good thermal contact to measure the temperature of the reference source, the uncertainty can be become lower than 1 %.

2.3.8 CCD camera

The benefit of using a CCD or CMOS camera is that you can look at the digital image it produces. This allows you to align the system in a very precise way, much more so than by eye when operating in the sub mm range. On top of this, you create an x-y grid of pixels and thereby creating a 2D heat map of the emitter. A typical setup of this scenario is shown in figure 2.9.

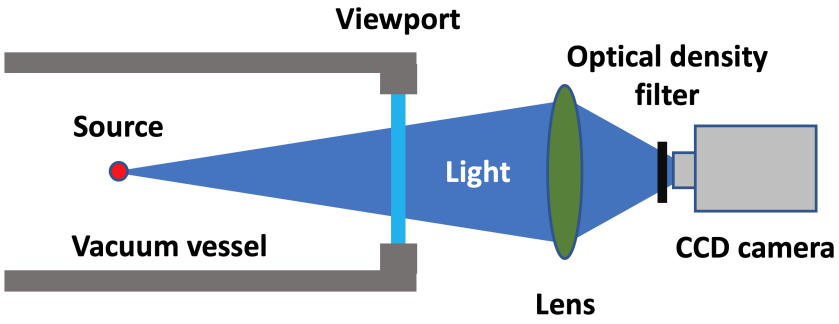

Figure 2.9: A typical setup of using a CCD camera to measure the intensity of the light of the source. The lens is used to create an image of the source on the CCD chip and the optical density filter is needed to stay within the dynamic range of the detector.

The process is very similar to single band pyrometry, but the radiance is measured using a CCD chip instead of a photodiode. This means that the multitude of different camera settings, i.e. exposure, shutter speed, camera software gain, will result in a difficult relationship between the radiance of the source and the measured signal.

Uncertainty

The use of a CCD camera for a temperature measurement cannot be done without absolutely calibrating the CCD chip. As this captures a broad band of wavelengths, the error is more difficult to calculate. Internal reflections and the dimension of the setup influence the intensity in a similar way as for the single band wavelength pyromotry setup. Better results could be achieved using a camera with red, green and blue pixels as that would give the relative differences between the intensities at different wavelengths instead of one intensity signal. There is no information of the variation in the signal over time. Nonetheless, both the monochromatic camera and the rgb camera would need to be absolutely calibrated before they can be used.

2.3.9 Emissivity for LaB_6 and Ta

For near-blackbody and greybody objects, the emissivities in equation 2.23 cancel out, but in the case of non-greybodies, the emissivities do affect the measurement. Both LaB_6 and tantalum have emissivities varying by wavelength.

Kowalczyk *et al.* have done emissivity measurements specifically for LaB_6 using a scanning grating monochromator setup[32]. Based on their research, figure 2.10 shows the emissivity of LaB_6 as a function of λ at a temperature of 1650 K.

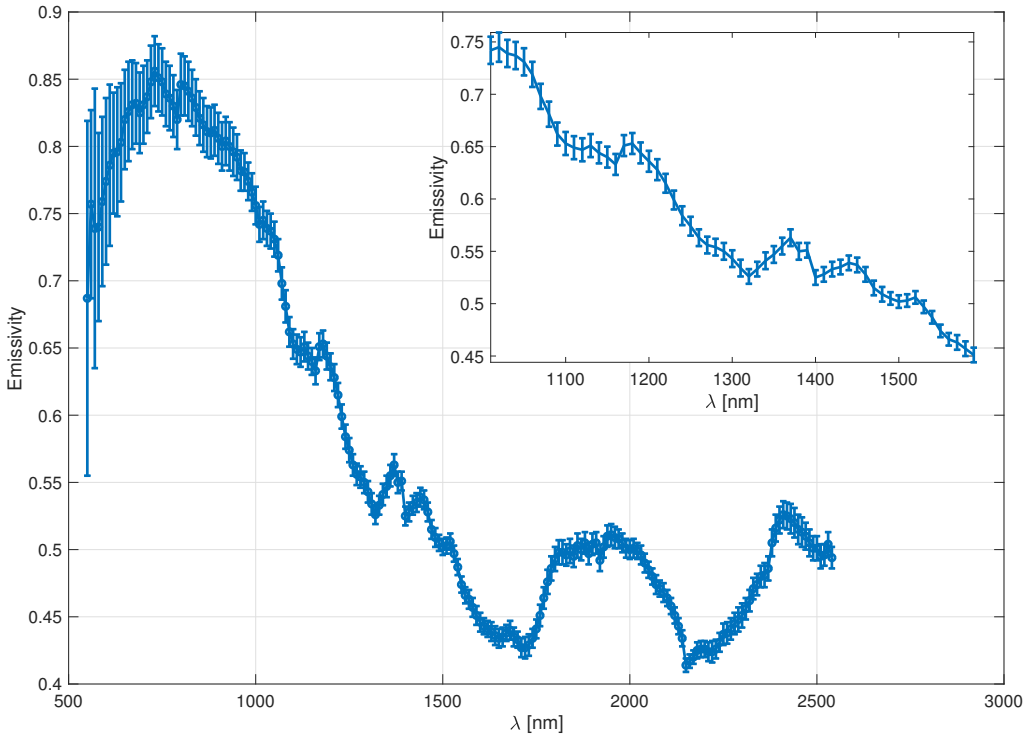

Figure 2.10: The emissivity of LaB_6 with error margins with a zoomed in plot of the wavelength range of interest. Data from [32].

All measured emissivity values in the range of wavelengths between 1050 nm and 1600 nm have a standard deviation of less than 2 %. Specifically for 1050 nm and 1550 nm (more on the choice of these wavelengths can be found in section 3.12), the standard deviations are 1.78 % for an emissivity of 0.731 and 1.27 % for an emissivity of 0.474 respectively. Therefore, with the data from figure 2.10 and equation 2.24, it is still possible to achieve a 2.27 % accuracy for the temperature measurement.

For tantalum, however, not the same level of detailed data is available. Literature states that the emissivity of tantalum with a polished surface is 0.47 for 1050 nm and 0.43 for 1550 nm[33], but there is no known standard deviation or error.

2.4 From continuous current to electron bunches

The emitter in the cathode emits a continuous electron current as is specified by equation 2.9, but the setup is meant to output short bunches of electrons. To go from a continuous beam to bunches, the continuous beam has to chopped and compressed. This is done using RF cavities.

2.4.1 Chopper cavity

The goal is to chop the beam with minimal loss of electrons and to maintain the quality of the original beam. Chopping with an RF cavity is typically done using one transverse magnetic field, but in this setup uses three transverse magnetic fields inside an RF cavity. Two magnetic fields are time-dependent and deflect the beam periodically and a static magnetic field is added to align the top of the sinusoidal wave, its maximum value, with the propagation axis along the z direction. When

the electrons exit the cavity they will travel through an aperture or a knife edge that only allows the on-axis electrons to pass through and will stop the deflected electrons. An illustration of this using a knife edge is shown in figure 2.11. Using the combination of time-dependent magnetic fields and a static magnetic field in the aforementioned configuration is optimal because of three reasons. Theoretically it results in no emittance growth for the electrons. Most electrons can be chopped out of the continuous beam at the peak of the sinusoidal wave. And third, the repetition frequency of the electron bunch train leaving the RF cavity is equal to the resonant frequency of the chopper cavity.

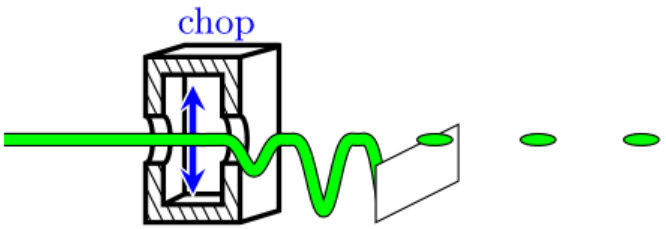

Figure 2.11: A schematic illustration of the chopping cavity[7]. The electron beam is indicated by the green line that is deflected by a time-dependent magnetic field, which is indicated by the blue arrow.

The electrons will only pass the knife edge when they are not deflected, i.e. when time-dependent magnetic fields and the static magnetic field counteract each other. For an ordinary sinusoidal wave, only about 1 percent of the electrons will pass the knife edge. This is too low to achieve a relevant charge per electron bunch as 99 percent of the initial beam is lost. To allow more electrons to pass, the magnetic field wave would have to be constant for as long as you would want the duty cycle to be. Ideally, this would be a rectangular wave, but this is practically impossible as it would require many modes inside the RF cavity. Adding only one higher harmonic mode however, also results in a flattened peak and thereby increasing the duty cycle. Figure 2.12 shows how combining the fundamental TM_{210} and second order TM_{230} mode results in a wave that has a relatively long and flat peak in the time domain[7]. TM_{210} and TM_{230} indicate waveguide modes for transverse magnetic waves, of which the magnetic vector is always perpendicular to the direction of propagation, resulting in only an electric field in along the direction of propagation. The suffix numbers attached to the mode type indicate the number of half-wave patterns across the x, y and z dimensions of the cavity[33]. Using the dotted part of the wave, the duty cycle can be increased to about 30 percent.

2.4.2 Compressor cavity

After the continuous beam is chopped into small stretches of electrons, these stretches will need to be compressed in order to be accelerated in an RF accelerator structure. This is done by the compressor RF cavity. The electrons in the cavity are accelerated and decelerated by a time-varying electric field in the propagation direction. The amount of acceleration or deceleration depends on the strength of the electric field and therefore the RF phase of the field inside the cavity. The electron bunch should be passing through the cavity when the electric field changes sign from plus to minus at the zero crossing and timing the entry of the electron bunches is very important. In this way the electrons in the back of the bunch will be accelerated and the electrons in the front of the bunch will be decelerated, while the electrons in the center of the bunch will not be affected by the electric field. By adding or taking away momentum of individual electrons depending on their position in this way, the electrons will start moving towards the center and thereby compressing the bunch. This concept uses the approximation of linearity at the zero crossing of a sinusoidal wave.

The beam exiting the chopper cavity has a duty cycle of 30 %. To compress these longer bunches, again a higher harmonic can be added to the cavity to improve the shape of the effective electric

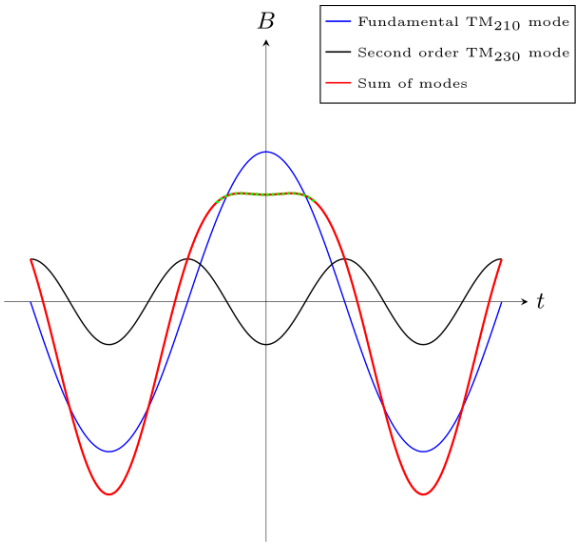

Figure 2.12: Superposition of the magnetic field modes resulting in the net magnetic field as a function of time to be used in the chopping cavity[7]. The sum of the modes results in a part of the wave to be relatively constant over time. This part is indicated by the green dotted line on top of the red line and is the part of the magnetic field that allows electrons to pass over the knife edge.

field wave in the desired way. Adding, in this case, a second order TM_{310} mode to the fundamental TM_{110} mode, results in a longer quasi linear part in the wave. This effect is shown in figure 2.13.

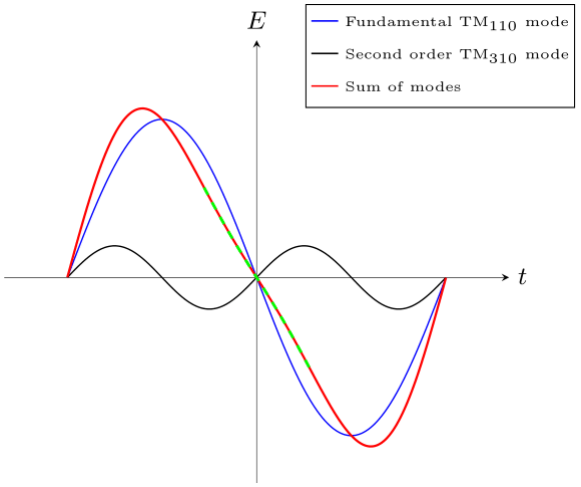

Figure 2.13: Superposition of electric field modes resulting in a net electric field to be used inside to compressor cavity[7]. The green dotted part on the red line indicates the linear part, with respect to time, that is used to accelerate and decelerate the electrons.

Both cavities together result in going from a continuous beam to a bunched output while maintaining roughly 30% of the electrons that were emitted by the electron source. Manipulating the electrons in this way should have minimal impact on the quality of the beam, but the magnitude of this effect will become evident in future experiments.

2.5 Focal planes

Working with multiple wavelengths requires taking a closer look at how these wavelengths pass through an array of lenses as they need to be focused on the photodetectors. The lens elements focus, collimate and reflect the light that goes through. Depending on the wavelength they will

interact with the light differently. The transmission and reflection spectra are shown in section 3.4.1 and will be discussed later. We will now focus on the theoretical basis for a potential challenge of the optics in this setup, the chromatic aberrations. The focal points of different wavelengths will be at different places. In figure 2.14 it can be seen how the refractive index changes with the wavelength that passes through the lens. The focal points can be calculated using the thick lens equation:

$$\frac{1}{f} = (n_l - 1)\left[\frac{1}{R_1} - \frac{1}{R_2} + \frac{(n_l - 1)\,d}{n_l R_1 R_2}\right], \tag{2.35}$$

with n_l being the index of refraction of the lens, R_1 and R_2 the radii of curvature for surfaces 1 and 2 (front and back) of the lens respectively, and d the center thickness of the lens. For a plano-convex lens R_1 is equal to ∞ and R_2 to $-R$. The minus sign in front of R results from the sign convention in the derivation of the thick lens equation. Then, equation 2.35 becomes

$$\frac{1}{f} = (n_l - 1)\left[\frac{1}{R}\right]. \tag{2.36}$$

The focal length of the lens calculated using equation 2.36 is the distance from the back principle plane to the point where the collimated beam is focused. To calculate the back focal length of the lens, also referred to as the working distance of the lens, we first need to calculate the back principle plane H using

$$H' = \frac{f\,(n_l - 1)\,d}{R_2 n_l}. \tag{2.37}$$

Using the same substitution $R_2 = -R$, equation 2.37 reduces to

$$H' = \frac{d}{n_l} = f - f_b, \tag{2.38}$$

with d/n_l, the edge thickness of the lens device divided by the refractive index of the lens, being equal to the distance between the effective focal length and the back focal length.

The second type of lens that is used is the bi-convex lens. For bi-convex lenses $R_1 = -R_2 = R$. This reduces equation 2.35 to

$$\frac{1}{f} = (n_l - 1)\left[\frac{2}{R} - \frac{(n_l - 1)\,d}{n_l R^2}\right]. \tag{2.39}$$

Using equation 2.37 and again the substitution $R_1 = -R_2 = R$, the back focal length can be calculated using

$$H = \frac{1}{\frac{(n_l-1)}{R} - \frac{2n_l}{d}}. \tag{2.40}$$

The back focal lengths are important, because we would like to image the emitter on the aperture to make sure only the light of the emitter reaches the detector. These images are not in the same plane. Furthermore, the system is aligned using visible light. As is also shown in figure 2.14 visible light sees a different refractive index and focuses in a different plane compared to both mentioned wavelengths.

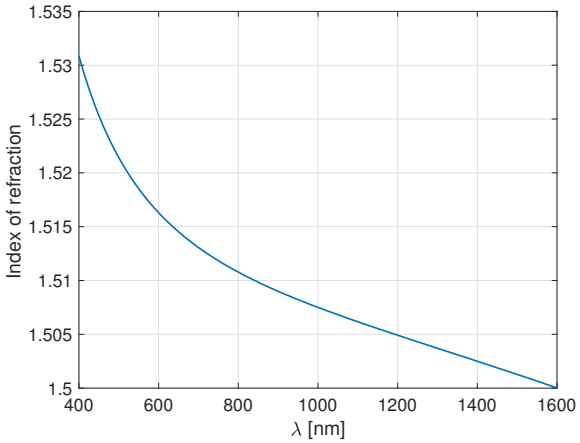

Figure 2.14: The refractive index of the lenses as a function of the wavelength.

Chapter 3

Experimental Setup

In this chapter the setup will be described in three main parts. First, the design of the thermionic gun and the beam line will be shown in more detail in sections 3.1 and 3.3. Then, the parts of the setup specifically used for the custom built dual wavelength pyrometer temperature measurement will be explained in section 3.4. The smaller setup for the other methods is shown in section 3.7.

3.1 Setup overview

The complete setup consists of several components, among which the electron emitter within the electron gun, the Faraday cup at the end of the beam line and the optical setup. Figure 3.1 shows how they are connected.

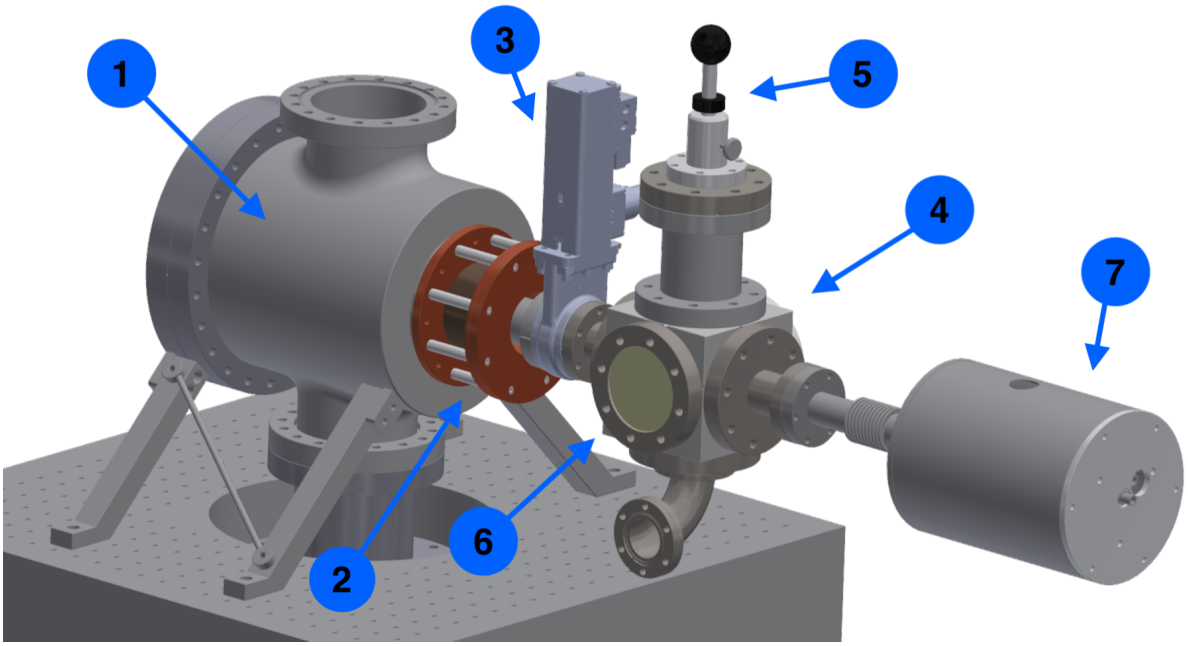

Figure 3.1: Overview of the beam line starting on the left with 1) gun vacuum housing, 2) the solenoid, 3) a vacuum valve, 4) a 63 mm cube, 5) an insert that holds the mirror inside the cube, 6) a viewing port and 7) the Faraday cup at the end.

The electrons are extracted from the electron emitter and accelerated by the electric field that surrounds the filament. How the electric field looks like is shown in section 3.2. Then, the solenoid is used to collimate the beam. The vacuum valve keep the vessel under vacuum while altering the beam line. The beam then passes through the hole in the center of the mirror, which is located in the cube, and continues towards the Faraday cup. The mirror enables us to see the electron emitter in the electron gun housing or the Faraday cup at the end of the beam line. Sight on the electron emitter is used for the measurement and sight on the Faraday cup is used to see whether the Faraday cup gets damaged due to the electron beam. The light from the electron emitter then goes through

the viewing window and is split into different wavelengths and guided to the detectors, which will be explained in section 3.4. The window is located at around 40 cm from the electron emitter. This is one of the restraints that make it more difficult to measure the temperature using a direct method. The electron beam continues towards the Faraday cup. Figure 3.1 does not show the steering coils, the vacuum pumps and the vacuum gauges. One set of four steering coils will be added before the cube to be able to steer the beam in the x- and y-direction. A turbomolecular pump is attached to the bottom of the vessel and a vacuum gauge is attached to the open port at the top of the vessel.

Future advanced include adding a blanker before the Faraday cup to deflect parts of the beam for future emittance measurements. Then, when the beam has been characterised, all elements in between the vacuum valve and the faraday cup will be replaced by the RF cavities. These are used to chop and compress the beam into electron bunches. The RF cavities are still being designed. They will be added at a later stage. This means that for now there is a continuous electron beam throughout the beam line that will be stopped by the Faraday cup. In the next sections the different components will be explained in more detail.

3.2 Thermionic Gun

The thermionic gun is shown in figure 3.2, which also shows the inside of the vacuum chamber with the cathode. The thermionic gun housing is a stainless steel vessel under vacuum that houses the electron emitter. The vacuum in the vessel reaches pressures of around 10^{-7} to 10^{-8} mbar. The housing is grounded and specifically designed to have the part at the front to function as the anode. The cathode is made of stainless steel, copper and titanium. Figure 3.3 shows a photo of the cathode when it is out of the vacuum chamber. The cathode is attached to the housing through the high voltage feed-through, which enables the power supply to supply 100 kV to the cathode. The power supply is able to deliver 100 kV with an emission current up to 10 mA as well as a heating current up to 4 A on top of the 100 kV. The cathode holds the electron emitter, which is shown in section 3.2.1.

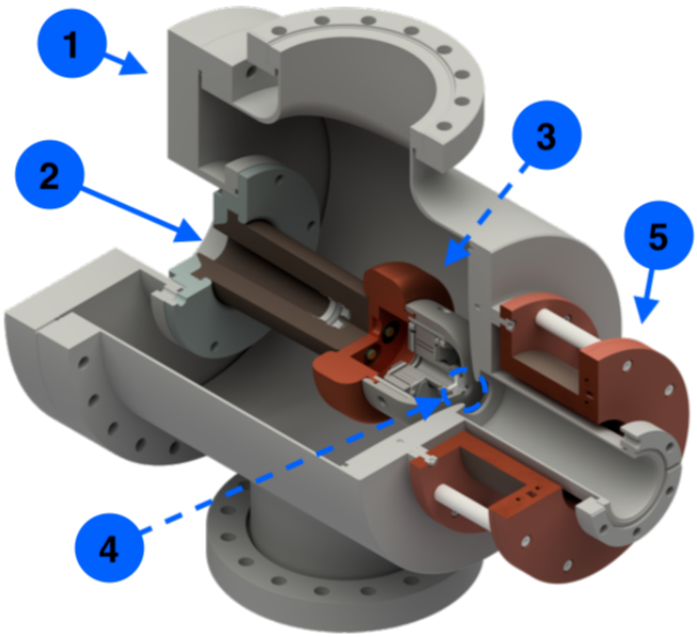

Figure 3.2: A CAD image of the thermionic gun with 1) the stainless steel housing, 2) the 100 kV high voltage feedthrough, 3) the cathode with 4) the electron emitter in it at the front, and 5) the solenoid.

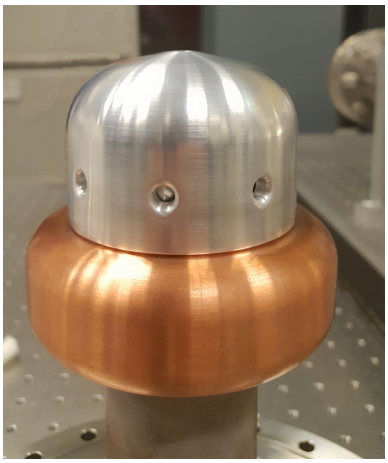

Figure 3.3: A photo of the cathode. The electron emitter is inserted in the top.

The shapes of the cathode and anode are made in such a way that they maximize the electric field at the electron emitter and minimize it elsewhere. The design enables the possibility of having a DC electric field of 10 MV/m at the surface of the emitter without breakdown. Figure 3.4 shows a more detailed CAD image of the design of the cathode at the place where the electron emitter is installed and how it is installed in the thermionic gun housing. Figure 3.5 shows a simulated image of the magnitude and the direction of the electric field at multiple positions in the $r - z$ plane. It is radially symmetric around the z axis. The most important thing to notice is that at the surface of the emitter the electric field is directed in the z direction.

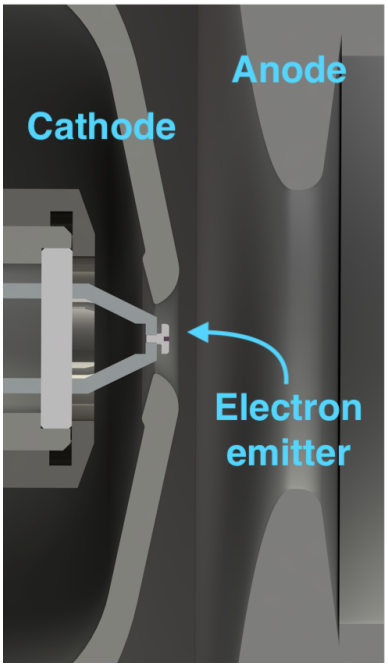

Figure 3.4: Side view CAD drawing of the cathode in the thermionic gun. A cross-section of the anode and the cathode, with the electron emitter inside, can be seen. It is radially symmetric.

Directly behind the anode a magnetic solenoid is attached to the vacuum vessel to control the transverse beam size. This is needed because the off-axis electric field is non-linear and has a component in the radial direction perpendicular to the direction of propagation, which causes the beam to diverge. With the magnetic solenoid this can be counteracted.

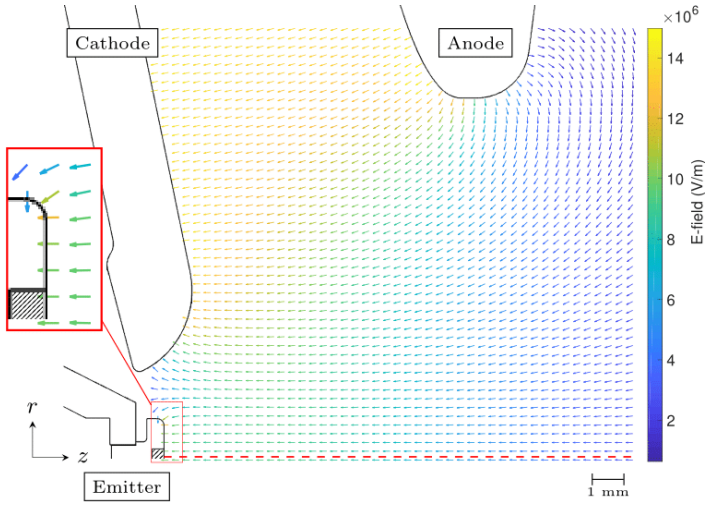

Figure 3.5: The simulated electric field around the cathode and the emitter in the $r - z$ plane. It is radially symmetric in around the z axis.

3.2.1 Electron emitters

LaB_6 electron emitter

The LaB_6 emitter is a disk with a flat polished surface and consists of a small piece of LaB_6 with a radius of 150 µm in the middle that is surrounded by a guard ring made of pyrolytic graphite. The crystal lattice of the LaB_6 emitter has a $< 100 >$ orientation and the guard ring functions as a holder as well as a resistive heating element. The sides of the pyrolytic graphite are rounded to create a smooth surface in order to minimize the electric field at the sides of the emitter. The graphite, including the LaB_6 in the middle, has a diameter of approximately 2 mm. Figure 3.6 shows an image of the emitter. The black part represents the graphite and the lighter grey area in the middle is the LaB_6 crystal, the part that emits the electrons.

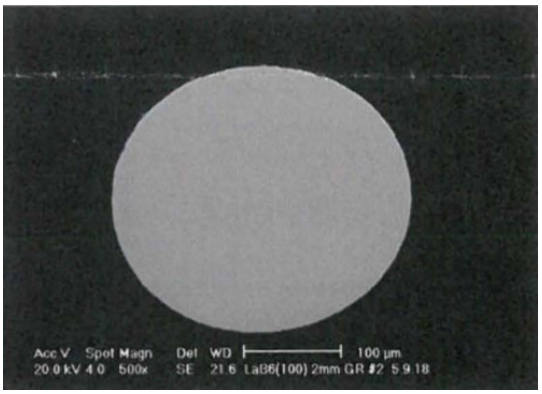

(a) An image of the LaB_6 electron emitter material inside the cathode.

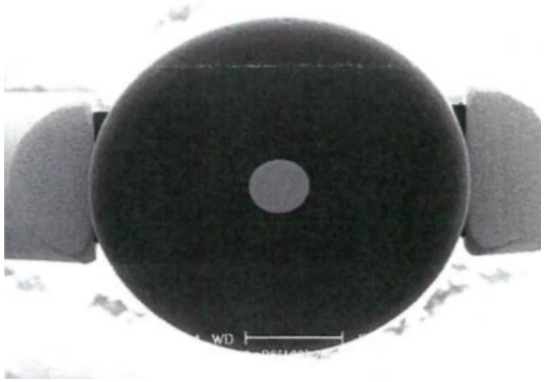

(b) A zoomed out image of the same object with the complete pyrolytic graphite edge and the supporting structure visible around it.

Figure 3.6: Images of the LaB_6 electron emitter material with the pyrolytic graphite guard ring in the Mini Vogel Mount structure.

This structure is mounted on a Mini Vogel Mount (MVM)^{TM}, which consists of two molybdenum-rhenium posts that maintain a high modulus of elasticity at high temperatures and a ceramic base[34].

The MVM feeds the the high voltage and the heating power supplied by the power supply to the emitter material and keeps it structurally stable at high temperatures. The Mini Vogel Mount is shown in figure 3.7.

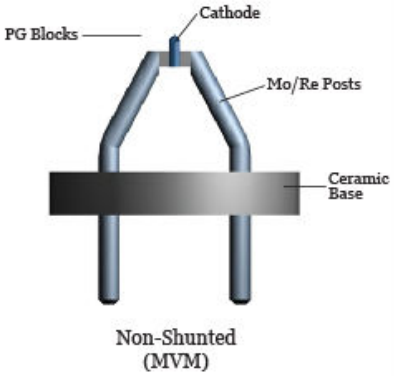

Figure 3.7: A schematic picture of the Mini Vogel Mount^{TM} holding a cathode[21]

The goal is to reach an emission current of 10 mA, which requires the emitter to be heated to 1760 K. Using equation 2.6 the Child-Langmuir limit can be calculated. With a distance of 10 mm between the cathode and the anode, a correction factor of 4.7 and at an electrostatic potential of 100 kV, the adjusted Child-Langmuir limit is calculated to be about 245 mA. Operation at 10 mA is therefore far below the space charge limit.

Tantalum cathode

Tantalum emitters are used as a cheaper alternative to the LaB_6 cathodes. The tantalum emitter has a flat polished surface with a round shape and a diameter of 0.84 mm. It has no pyrolytic graphite guard ring in contrast to the LaB_6 cathode. The work-function of the cathode is 4.1 eV and its potential emission current is 1 mA. For this, a heating current between 1.4 to 1.8 A is required depending on the specific dimensions of the emitter. At these currents the tantalum emitter typically has a temperature of 2200 K. Figure 3.8 shows a CAD image of the tantalum disk cathode on a ceramic base.

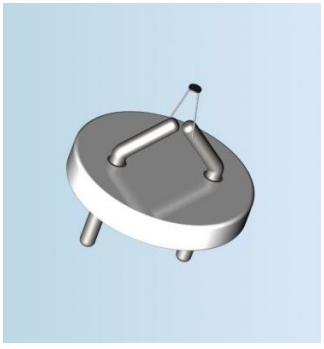

Figure 3.8: CAD image of the Tantalum Disk Cathode[35].

3.3 Beamline

Attached to the thermionic gun are several more components. Directly behind the solenoid on the gun there is a 63 mm CF cube with a 5.08 cm by 5.08 cm mirror inside it to reflect the light from the LaB_6 cathode through the viewing port to outside the vacuum system. The mirror is 6 mm thick and has an unprotected gold layer on it to optimally reflect the IR wavelengths ranging from 800 nm to 20 µm. In the center of the mirror there is a 4 mm hole to let the electron beam pass through it. Figure 3.9 shows a render of the mirror. The other ports of the cube serve for another vacuum pump and another vacuum gauge at the bottom, a viewing window and the insert at the top holding the mirror. Then there is a set of steering coils to direct the beam to the Faraday cup. It is attached right before the cube to steer the x- and y-direction of the beam.

This beamline is designed to investigate experimentally what the relationship is between the emitter current and the emitter temperature and to compare this with the Richardson's equation for thermoinic emission, equation 2.5. First for the tantalum emitter and in the future for the LaB_6 emitter.

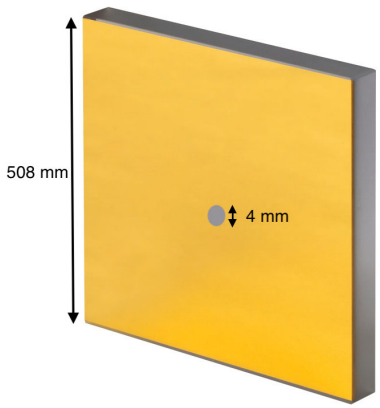

Figure 3.9: An illustration of the square mirror with the 4 mm hole in the middle[36].

3.3.1 Faraday cup

At the end of the beam line the electron beam has to be stopped. This is done using a water-cooled Faraday cup. As the desired current is 10 mA at 100 kV, the total power absorbed by the Faraday cup is ∼1 kW. In order to dissipate this heat it has water flowing through channels in its housing. Furthermore, as the high energy electrons hit the copper, radiation is produced in the form of X-rays, the characteristic radiation and photo-emission for copper at around 6 keV photons and brehmsstrahlung up to 100 keV photons, and secondary electrons. Most of the secondary electrons will be reabsorbed and the copper shields for the X-rays by reducing the intensity of the X-rays by 50 % every 1.8 mm for 100 keV photons. However, at the entrance of the Faraday cup there is no shielding. How much radiation will be measured outside and at the entrance of the Faraday cup will have to be measured experimentally.

The Faraday cup is also used as a safety measure. The emission current is known and the Faraday cup measures the beam current at the end of the beam line, meaning the difference in current is lost throughout the beam line. When this difference becomes too large, the electron gun will be shut down. The difference limit is determined by how much radiation is produced.

3.4 Optical system

In the custom built dual wavelength pyrometer the black body radiation emitted by the electron emitter (LaB_6 or tantalum) is reflected by a mirror and sent to the photon detector through a series of optical elements. The reflected light from the mirror is split into two directions, after which two specific wavelengths, 1050 nm and 1550 nm, are filtered out using narrow-band filters and sent to the InGaAs detectors. More on the choice of wavelengts will be explained in section 3.4.2. A schematic overview of the optical setup used in this experiment is shown in figure 3.10.

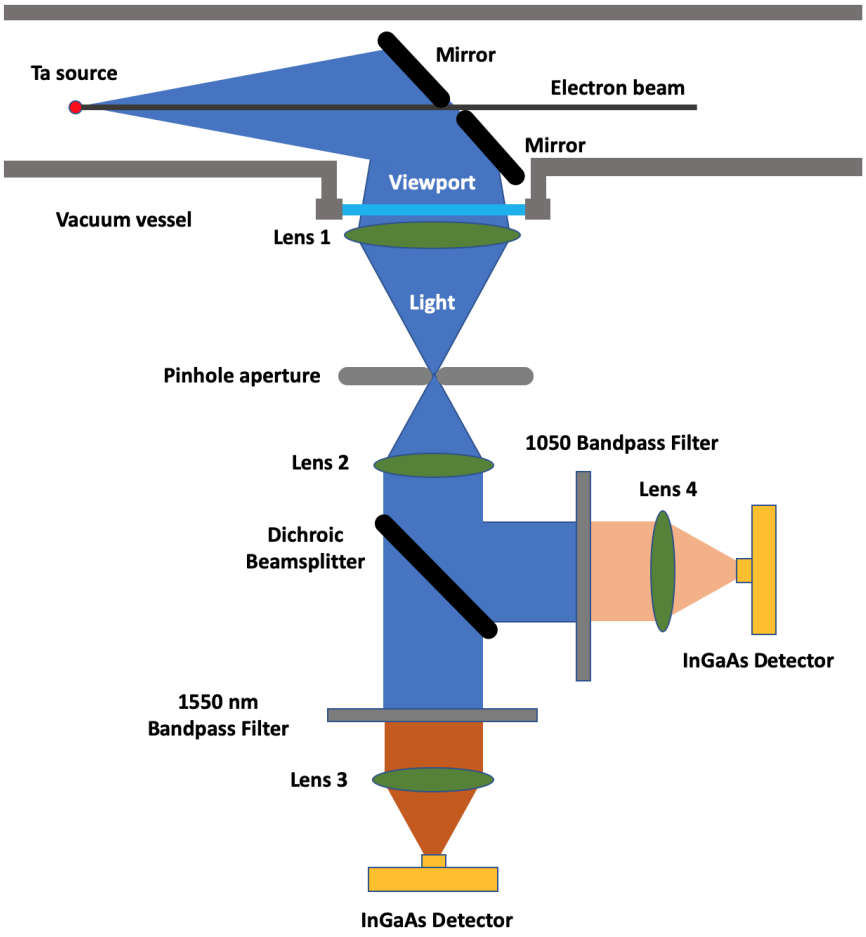

Figure 3.10: The optical setup used in this experiment. The light comes from the electron emitter in the top left corner and then goes through a series of optical elements, after which two specific wavelengths reach two different detectors.

3.4.1 Components

The first object the light coming from the electron emitter sees is the mirror. This is a 5 cm by 5 cm unprotected gold coated mirror specifically meant for reflecting infrared wavelengths. The gold coated mirror has a reflectance of 97.8 percent for 1050 nm and 98.3 percent for 1550 nm[36]. Then the light goes through the viewing window of the vacuum chamber, which has a measured transmission of 98.5 percent for both 1050 nm and 1550 nm, towards the first lens, lens 1. An overview of the lenses used and their properties is shown in table 3.1. An aperture is placed between lens 1 and lens 2 to block the light from the graphite structure surrounding the LaB_6 material. The magnification of the emitter at the image plane after the first bi-convex lens is calculated to be 0.27x. With an object size of 300 µm for the original LaB_6 emitter, the image size will be 81 µm at the

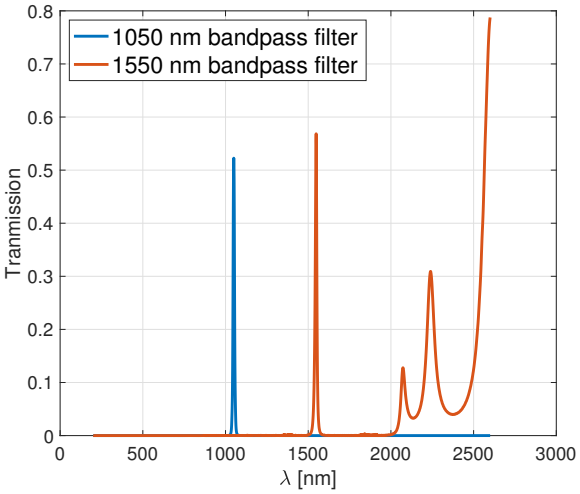

(a) The transmission curves of the narrow band-pass filters[37].

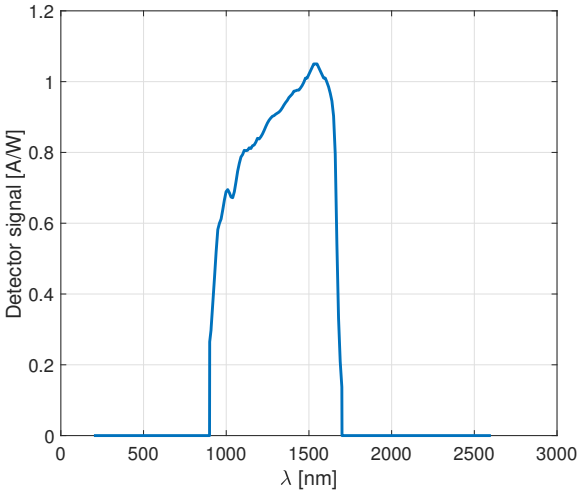

(b) The sensitivity of the photodiode in the GaInAs detector[38].

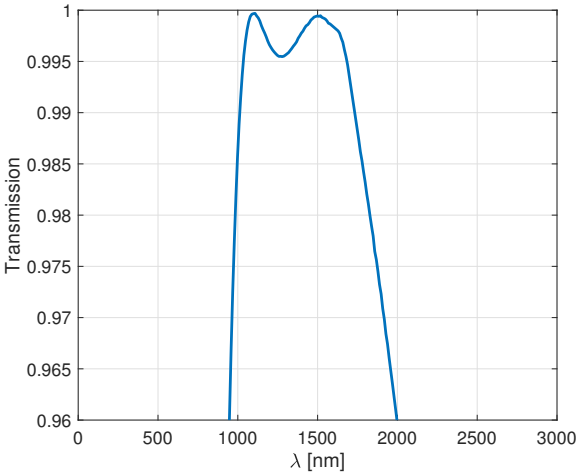

(c) Transmission curve of the lenses[31].

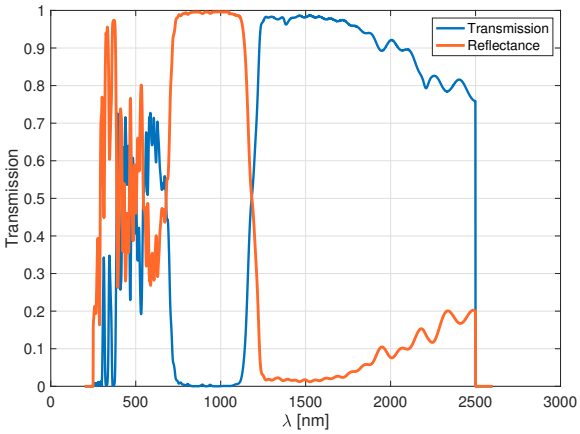

(d) Transmission of the dichroic mirror[36].

Figure 3.11: An overview of the optical components in the experimental setup.

image plane where the aperture is located. This requires the aperture to be smaller than 81 µm. The aperture in the experiment has a diameter of 50 µ. Then, lens 2 is used to collimate the remaining light. The light then passes onto a dichroic beam splitter placed at an angle of 45 degrees, which reflects 99.1 percent of the light at 1050 nm and transmits 98.2 percent of the light at 1550 nm to separate the two wavelengths. After the dichroic mirror the used wavelengths are selected using two different narrow-bandpass filters for both wavelengths. The first narrow band-pass filter has a center wavelength of 1050 ± 2 nm with a full width half maximum (FWHM) of 10 ± 2 nm. The second filter has a center wavelength of 1550 ± 2.4 nm and a FWHM of 12 ± 2.4 nm. The band-pass filter need to be placed perpendicular to the incident beam of light. Rotating these filter about 10 degrees will shift the center wavelength about 5 to 6 nm, depending on the starting center wavelength. The light then goes through lens 3 and 4 that focus the light on two individual photo detectors at the end. The photo detectors are made of InGaAs with a surface area of 0.8 mm^2 and are sensitive from 900 to 1700 nm. The transmission spectra of the different aforementioned optical components are shown in figure 3.11. The distance from the emitter to the first mirror is 44 cm.

Table 3.1: Overview of the lenses and their properties[31]. The numbers of the lenses correspond to figure 3.10.

Lens	Material	Diameter	Type	Coating	Focal length
1	N-BK7 optical glass	5.08 cm	Bi-convex	AR 1050 to 1700 nm	100 mm
2	N-BK7 optical glass	2.54 cm	Plano-convex	AR 1050 to 1700 nm	35 mm
3	N-BK7 optical glass	2.54 cm	Plano-convex	AR 1050 to 1700 nm	35 mm
4	N-BK7 optical glass	2.54 cm	Plano-convex	AR 1050 to 1700 nm	35 mm

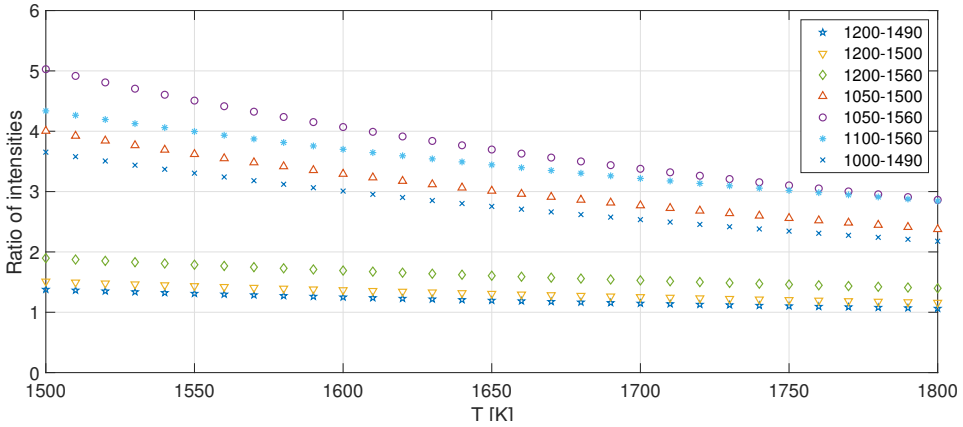

Figure 3.12: Ratios of intensities for different combinations of wavelengths in nm for different temperatures.

3.4.2 Choice of wavelengths

Dual wavelength pyrometry is based on the ratio of two different wavelengths and therefore the choice of wavelengths is based on maximizing the change in the ratio as the temperature changes, while also maintaining a good signal. As was mentioned earlier, the infrared range has been chosen because that is the range where the intensity of the blackbody radiation is the highest. In this range however, there are still many wavelengths to choose from.

Figure 3.12 shows different combinations of wavelengths and the ratios of their intensities as a function of temperature. The wavelength range in the figure is chosen based on what is easily commercially available. Also taking into consideration the wavelength range of the detector and other optical components, 1050 nm and 1550 nm were chosen as the best option.

3.4.3 Processing

The known transmission spectra as shown in figure 3.11 are used to calculate the losses of the radiation as it passes through the optical system shown in figure 3.10. Figure 3.13 shows how the light intensity changes as it goes through the optical system. For 1800 K the ideal black body radiation, the relative detector signal of the spectrum after the transmission losses of the optical components and the light that reaches the detector after the 1550 nm narrow band-pass filter are plotted. The intensity of the black body radiation is normalized for this example. The emissivity from figure 2.14 is also taken into account.

The signal coming from the Thorlabs InGaAs detectors is read by two independent Keithley current meters that can measure down to 10 nA. When 10 nA is not low enough, another Keithley current meter is used that is capable of measuring pA. The current output I_{out} from the photodiodes measuring wavelength i is given by

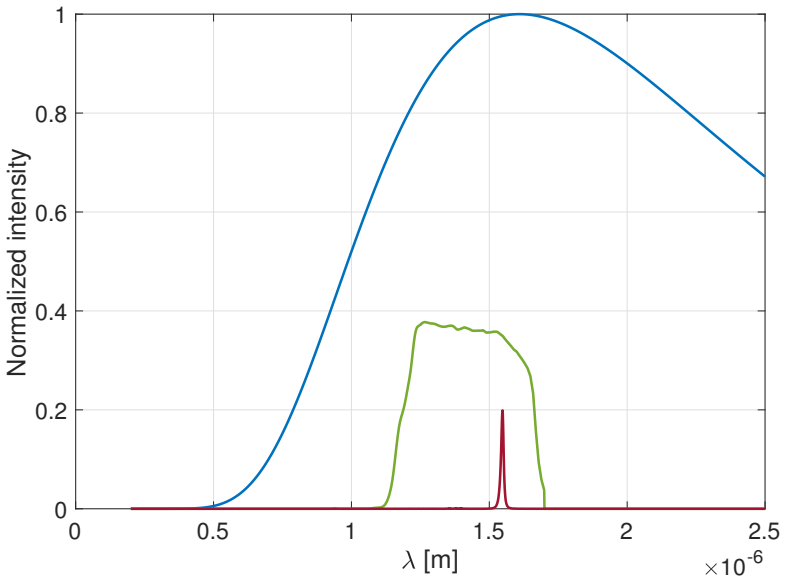

Figure 3.13: The normalized intensity of the black body radiation for 1800 K based on 1) the ideal black body radiation in blue, 2) The relative detector signal of the spectrum based on its responsivity curve after the transmission losses of the optical components in green and 3) The amount of light that reaches the detector as a result of the 1550 nm narrow band-pass filter in red.

$$I_{\text{out},i} = I_0 + E(\lambda_i, T) \cdot \tau_{\text{lens}}(\lambda_i)^3 \cdot \tau_{\text{viewport}}(\lambda_i) \cdot \tau_{\text{beamsplitter}}(\lambda_i) \cdot \sigma_{\text{filter}(\lambda_i)} \cdot S(\lambda_i), \tag{3.1}$$

with I_0 being the dark current when there is no illumination. The dark current is below 2 nA[38] and is accounted for in the measurements.

Uncertainty

Practical sources of errors are the alignment of the target spot on the emitter crystal, distinguishing the heater element from the emitter crystal and the true emissivity values for both the LaB_6 and tantalum emitters at the specific wavelengths and temperatures.

The largest component of the uncertainty in the measured intensity is due to the alignment, but there is also an error from the optical components. The components introduce a systematic error due to the variation in the manufacturing process and the detector introduces a random error. The error without calibration for the setup shown in figure 3.10 is calculated as follows:

$$\delta I_{\text{det}} = I_{\text{det}} \sqrt{\left(\frac{\delta\epsilon}{\epsilon}\right)^2 + 3\left(\frac{\delta\tau_l}{\tau_l}\right)^2 + \left(\frac{\delta\tau_{bs}}{\tau_{bs}}\right)^2 + \left(\frac{\delta\tau_m}{\tau_m}\right)^2 + \left(\frac{\delta\tau_{vp}}{\tau_{vp}}\right)^2 + \left(\frac{\delta\tau_f}{\tau_f}\right)^2 + \left(\frac{\delta R}{R}\right)^2}, \tag{3.2}$$

in which τ_f is the transmission of the filter and τ_l the transmission of the lenses. The emissivity error from the data in figure 2.10 is 1.78 percent and for tantalum the error is unknown. For the calculation we will use a 3 percent error. The error from the Thorlabs singlet lenses with the IR AR coating have a variation in transmission of 0.8 percent. The uncertainty for reflectance and transmission of the beamsplitter is estimated to be 2 percent. The uncertainty of the mirror and the viewpoint are unknown, but seeing it as equal to the coating on the lenses an uncertainty of 0.8 percent will be

used. The uncertainty for the sensitivity of the Thorlabs photodetectors is also unknown. For this we will assume 2 percent. The band-pass filters have an uncertainty of 2.4 percent. Using these error percentages and equation 3.5 the uncertainty is

$$\frac{\delta I_{\text{det}}}{I_{\text{det}}} = \sqrt{(0.03)^2 + 3 \cdot (0.008)^2 + (0.02)^2 + (0.008)^2 + (0.008)^2 + (0.024)^2 + (0.02)^2} = 0.051 \quad (3.3)$$

It is the ratio of two current signals that results in a temperature and the ratio does not scale linearly with the temperature. To calculate the temperature uncertainty, equation 2.32 can be used to find the percentage deviation in the temperature as a result of different currents of the uncertainty range. An uncertainty of 5.1 % in the ratio of the two current signals results in an uncertainty of 4.7 % in the temperature reading at a temperature of 2200 K for tantalum. Furthermore, when the ratio of the two is taken, the assumption is that the error will be smaller than 4.7 %, but for now we will take the maximum as the error in the temperature measurement. At an operational temperature of 2200 K, 4.7 % is equal to an error margin of ± 103 K. By calibrating the setup using a reference source the error can be decreased. This is described in Section 3.6.

3.5 Chromatic aberrations

Another contributor to the measurement error in the setup with the aperture for LaB_6 are the chromatic aberrations. The optical elements focus, collimate and reflect the light that is captured by the first lens. Depending on the wavelength they will interact with the light differently. This is important as we would like to image the emitter on the aperture to make sure only the light of the emitter reaches the detector. Chromatic aberrations cause the emitter to be imaged in different focal planes for both wavelengths.

Using equations 2.36 and 2.38 the focal and back focal lengths are calculated. With a radius of curvature of 18.0 mm for the plano-convex lenses, this results in a focal length of 35.51 mm for $\lambda = 1050$ nm and 35.96 mm for $\lambda = 1550$ nm. The edge thickness of the used lens is 2.0 mm. Hence, the back focal lengths of the lens are 34.62 mm for $\lambda = 1050$ nm and 34.19 mm for $\lambda = 1550$ nm. Chromatic aberrations therefore lead to a difference in back focal planes of 0.43 mm. This is a small difference and can be overcome by adjusting the positioning of the detectors through maximizing the signal.

The chromatic aberration error is more important for the bi-convex lens, which focuses the light onto the aperture. As has been said, the different focal points create an image of the emitter at different planes when looking at different wavelengths. For a bi-convex lens with a radius of curvature of 101.4 mm the focal lengths can be calculated using equation 2.39. This results in a focal length of 100.53 mm for $\lambda = 1050$ nm and 101.78 mm for $\lambda = 1550$ nm. Both back focal lengths can be calculated using equation 2.40 and are found to be 99.53 mm for $\lambda = 1050$ nm and 100.77 mm for $\lambda = 1550$ nm, with the difference between the two being 1.24 mm. This results in a difference of 1.46 mm in the image distance of the setup.

When placing an aperture of 50 µm, the distance of 1.46 mm between the focal planes affects the ratio of the amount of the light that can pass through the aperture for 1050 nm and 1550 nm. If the 1050 nm wavelength were to be focused, the image would be misaligned for the other wavelength, resulting in a disturbed ratio of the intensities and a measurement error. When the aperture is aligned with the focal plane of the 1050 nm light, the ratio would be 11 times smaller compared to the ratio when no aperture is used. Figure 3.14 illustrates the effect of the chromatic aberrations in

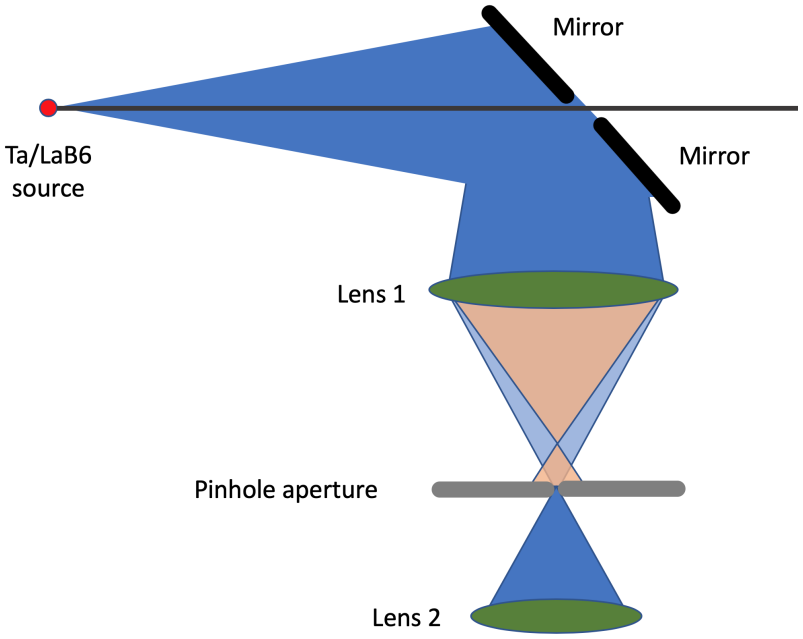

Figure 3.14: An illustration of the chromatic aberrations in the optical setup (not drawn to scale).

combination with the aperture. During the measurements the setup can be aligned using 1050 nm, which is still visible using a CCD camera, and then changing the location of the aperture by 1.46 mm using a translation stage when measuring at 1550 nm. Another way to do this is to calibrate the setup after it has been put in place and aligned. That way the disturbed ratio is taken into consideration, thereby taking away the error of the chromatic aberrations.

3.6 Calibration

The individual components with unknown transmission spectra have to be calibrated in order to use the method in section 2.3.6. A quartz tungsten-halogen lamp is used to calibrate the unknown optical components, such as the viewing ports in the vacuum systems, specifically for 1050 nm and 1550 nm using the same narrow band-pass filters that are used in the setup. Some of the used components have wavelength dependent transmission data from the suppliers and some are unknown. The emissivity of the LaB_6 emitter is known for similar, but not the exact same, conditions and shown in section 2.10. The emissivity for the tantalum emitter has not been calibrated and even though there can be found values in literature that can be and are used, this is a source of an unknown error.

The complete setup can also be calibrated using a reference source. When calibrated for one or more known temperatures, the uncertainty of the temperature measurement can be decreased. The calibration of the dual wavelength pyrometry setup as a whole has been designed, but has not yet been built.

3.6.1 Calibration setup

The current accuracy of the measured temperature is influenced by several factors that have been discussed in section 3.4.3. Most of all, it is the alignment of the optical components that changes the outcome of the measurement. On top of this, the change in emissivity greatly influences the

intensity of the light that is radiated and because this is wavelength-dependent, it affects the ratio measurement through which the temperature is determined.

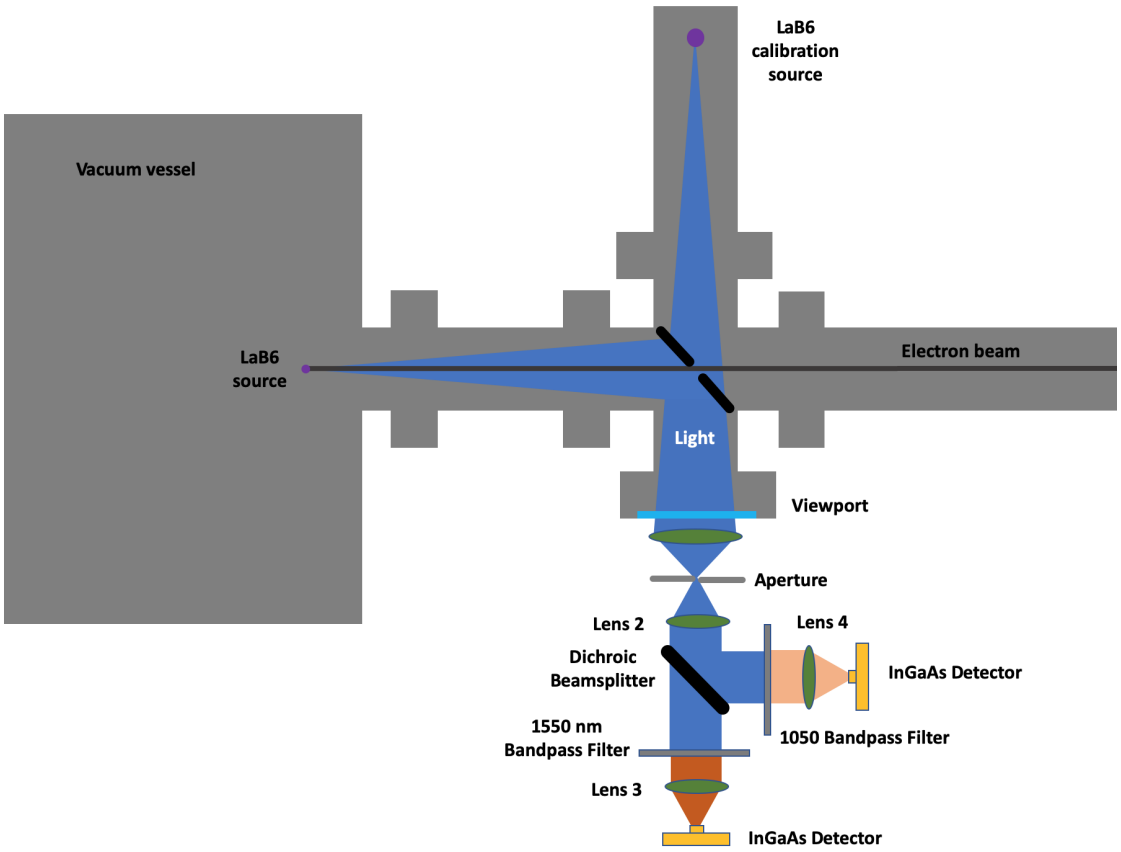

Figure 3.15: The calibration setup that is incorporated in the beamline. The original LaB_6 emitter in the cathode is shown on the left and the calibration emitter is indicated by the larger purple circle in the top of the figure. The optical setup is identical to figure 3.10.

To take away the uncertainty of both of these factors, the optical system can be calibrated after being installed and aligned. This is done using another LaB_6 emitter with the same polished surface and fabricated by the same manufacturer at the position shown in figure 3.15. Calibrating for tantalum is not of interest for the project, for it is used as a test emitter with other purposes. By placing the calibration setup into the beamline the alignment of the optical components does not have to be changed. This way, the system is calibrated as a whole and the errors of the individual components are not relevant anymore. Only the error in the reflectivity of the mirror is left as the mirror is the only thing that is inserted in or taken out of the light path. The main contribution to the error will then be the temperature measurement of the calibration emitter, which can be done more precisely using a high temperature thermocouple as it does not have the limiting constraints the emitter in the cathode has. Figure 3.15 shows how the calibration setup can be incorporated into the beam line, so that the calibration can be done after alignment. The high voltage cathode with the emitter is located on the left inside the gun. The calibration emitter is placed perpendicular to the beamline at exactly the same distance as the emitter in the cathode. Then, only the mirror has to be pulled out of the beamline in order to start the calibration. The LaB_6 calibration emitter is 3 mm in diameter, which is 10 times as large as the LaB_6 emitter in the cathode of the gun. This has two advantages. The normal electron emitter in the cathode is too small and fragile to be pressed against a thermocouple, but the size of the calibration emitter makes it easier to handle. Therefore the temperature of this piece can be measured using a high temperature type B thermocouple, which is capable of measuring up to 1900 K, and is placed in direct contact with it. This ensures an accurate temperature measurement to base the calibration on. Secondly, the bigger surface area means that it

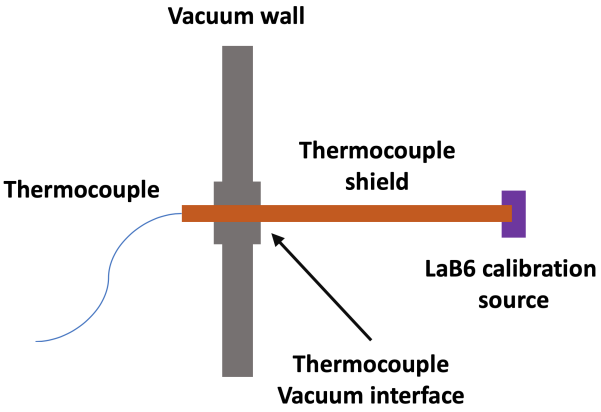

Figure 3.16: A schematic overview of how the calibration source would be measured using a thermocouple and how the thermocouple is attached to the vacuum vessel.

is easier to align the optical components. The emitter does not have to be placed as precisely and as it is a ratio measurement, the area of the spot size does not affect the outcome of the measurement. The temperature measurement is only based on the intensity ratio of two specific wavelengths and that is a very useful property of dual wavelength pyrometry. The disadvantage is that it needs more energy to heat up and due to the larger contact surface more energy will leak out of the system.

Temperature error

A thermocouple has the lowest error in the temperature readout at temperatures around 1700 K and therefore it has been chosen to measure the reference temperature. At temperatures of more than 1600 K, the only type of thermocouple that is capable of going to such high temperatures (up to 1900 K) is type B. Type B consists of two alloys, one platinum with 30 % rhodium wire and a platinum with 6 % rhodium. The purity of the material determines the error and using special limit materials the error of these thermocouples is 0.25 %[39].

Thermal conduction

The calibration emitter will be placed in a vacuum environment. Therefore the heat loss due to convection is practically zero, but there will be radiative losses and heat will dissipate through the supporting structure. How exactly this support structure will look like still has to be designed, but for now we will take the thermocouple as the heat sink. The used thermocouple has a diameter of 3 mm and will be in contact with both the hot calibration emitter and the colder vacuum housing. Thus a temperature gradient will exist. Even though the thermocouple joint itself is capable of heating up to over 2000 K, the electrically isolating cement is rated at 1900 K and the seal at the end only at 630 K. It is therefore important to know the heat transport from the LaB_6 material across the molybdenum sheath to the Swagelock vacuum interface and the seal on the other end of the thermocouple. The described situation is visualized in figure 3.16. In this case the LaB_6 emitter is supported by the thermocouple, but the heating wires or elements are not shown.

An estimate for the heat transfer across the sheath can be calculated using

$$\frac{Q}{t} = \frac{kA\Delta T}{d}, \tag{3.4}$$

in which k is the thermal conductivity of the material, A the area of a cross section of the sheath and d is the length of the sheath. With k being 120 $\mathrm{Wm^{-1}K^{-1}}$ for molybdenum and using a surface of 0.06 $\mathrm{cm^2}$ and a distance of 10 cm between the tip and the seal at the back, equation 3.4 indicates that there is a constant transfer of heat of 10 W in case of a temperature difference of 1400 K between the two ends. This could be absorbed by the vacuum structure acting as a heat sink or could be cooled using active cooling such as water cooling.

3.7 Other methods

3.7.1 Use of spectrometer

To prove the feasibility of using black body radiation as a method to determine the temperature, the initial idea was to capture the tail of the black body spectrum in the 200 to 1100 nm range, as this was the only range there was a detector available for. By fitting the shape of the curve to the data points, the temperature could be determined.

To try the aforementioned approach, a 1kW light bulb was used as a source, which was powered by a variable power supply to change the temperature of the filament inside. The temperature characteristics were unknown, but the temperature of the filament would range from several hundreds up to 3000 K, depending on the amount of power put in[40]. However, the measured spectrum only changed in intensity, which is expected, but not in shape at all. Furthermore, fitting the black body curve gave unrealistic results and so we continued the exploration with a better approach.

The actual temperature of the filament inside the light bulb was unknown and visible light was scattered from all around the detector. Hence, we created a dark environment with a wire in vacuum that was wrapped around a thermocouple. This way we could measure the temperature of the wire in a different and accurate way and only that light would fall onto the detector. By running a current through the wire, power will dissipate as heat and the wire will heat up. Its black body radiation then scales with its temperature as T^4.

In figure 3.17 an overview is given of what visibly happens to the wire as it heats up. The photos show the color of the wire at different currents running through the wire and thus different temperatures. Two things can be observed. First, the color changes from red-ish in figure 3.17a to yellow-ish in figure 3.17e. Second, the intensity changes as is also clearly visible in reflection of the wire on the inside of the vacuum chamber and towards the corners of the photos, which are taken with the same exposure settings.

For this setup the spectrometer again showed different spectra only changing in intensity and not in shape, even though we have optically established that there is a noticeable color shift as the temperature of the light filament increases. An example of a spectrum that has been measured at 800 K is shown in figure 3.18. The spectrum corresponding to that of an ideal black body ($\varepsilon = 1$) with a temperature of around 800 K is included as reference, as what the shape of the measured curve should resemble. As can be seen, the spectrum of the spectrometer starts going up in counts just after 500 nm, while the expected black body spectrum does not start to increase significantly until towards 800 to 900 nm. Only when the temperature increases more, the peak of the black body curve starts shifting towards 900 nm.

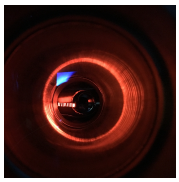

(a) 600 K

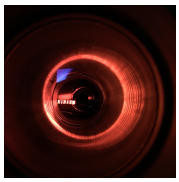

(b) 680 K

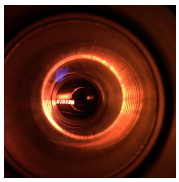

(c) 760 K

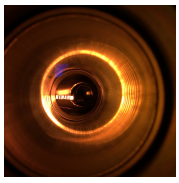

(d) 840 K

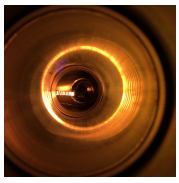

(e) 900 K

Figure 3.17: Photos of the glowing wire at different temperatures.

For the peak to be at 900 nm or smaller, the temperature needs to be 3000 K or higher. It could also be that the thermocouple is not making good thermal contact with the wire and therefore not giving an accurate temperature reading. That way the wire has a higher temperature than we think it has and the spectrum is misinterpreted. Nevertheless, the spectrometer's sensitivity range up to 1100 nm seems unusable for these experiments. An IR spectrometer is not available and is out of budget. That is why the dual wavelength pyrometer is developed.

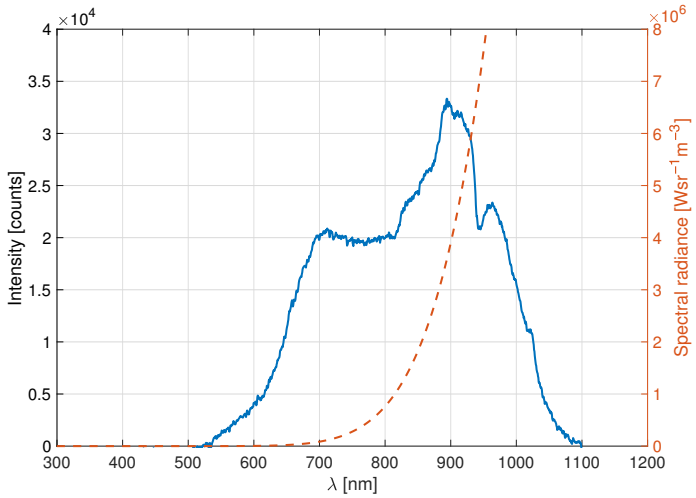

Figure 3.18: Measured spectrum of glowing wire and ideal black body spectrum for 800 Kelvin.

3.7.2 Quartz tungsten-halogen lamp

A test setup had been built before the beamline was finished to test the feasibility of single band pyrometry and the dual wavelength pyrometry setup. For this, a Thorlabs quartz tungsten-halogen lamp with broadband emission from 400 to 2200 nm has been used. An 150 µm aperture has been placed in front of it to set the size of the source as this is an important parameter for single band pyrometry. Figure 3.19 shows an illustration of the setup, which closely resembles the setup shown in figure 2.7. A single 35 mm lens, lens 2 from table 3.1, the same InGaAs detector and 1550 nm narrow band-pass filter from the dual wavelength pyrometry setup described in section 3.10 have been used. The emissivity of tungsten is 0.28 and the solid angle of the setup is calculated to be 0.000177 using the area of the aperture and the distance from the first lens to the emitter.

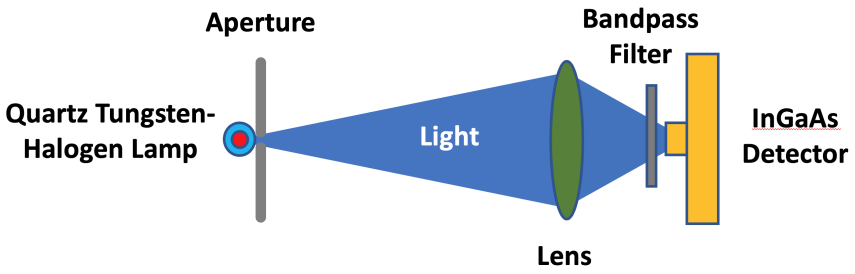

Figure 3.19: Initial setup to test the feasibility of the built setups, using a Quartz Tungsten-Halogen Lamp, an aperture, a 35 mm lens with IR AR coating and an InGaAs photodetector.

The quartz tungsten-halogen lamp has an indicated temperature of around 2500 K. By placing an aperture with a 150 µm diameter in front of the lamp it was more similar to the real emitter crystal

scenario and a well defined area of emittance contributes to a more accurate reading. The lamp is attached to a 12 V power supply delivering about 10 W of electrical power.

For the dual wavelength measurement, the same setup as is shown in figure 3.19 is used, but instead of a single detector there are two detectors on the right side of the lens, just like is shown in section 2.8). Everything to the left of the lens, meaning the quartz tungsten-halogen lamp and the aperture, remain the same.

Uncertainty

The standard deviation can be calculated as is done in section 2.3.5. For the components used in figure 3.19 this becomes

$$\frac{\delta I_{\text{det}}}{I_{\text{det}}} = \sqrt{\left(\frac{\delta\Omega}{\Omega}\right)^2 + \left(\frac{\delta A_{\text{source}}}{A_{\text{source}}}\right)^2 + \left(\frac{\delta\epsilon}{\epsilon}\right)^2 + \left(\frac{\delta\tau_{\text{lens}}}{\tau_{\text{lens}}}\right)^2 + \left(\frac{\delta\tau_{\text{filter}}}{\tau_{\text{filter}}}\right)^2 + \left(\frac{\delta R}{R}\right)^2}, \tag{3.5}$$

in which $\delta\epsilon$ includes the emissivity in combination with the transmission loss of the source enclosure. The area of the light emitting source is approximated with an aperture that is close to it, but the dimensions of the tungsten emitter inside the housing are unknown and due to the distance of between the aperture and the filament, more light could go through then is estimated. It could be 1 mm long or 0.7 mm long and the same uncertainty is applicable for the width of the filament. Therefore the uncertainty for the emitter area in combination with the solid angle is taken as 30 % for the quartz tungsten-halogen lamp. The uncertainty of the emissivity and the transmission of the enclosure are estimated to be around 8 %. The uncertainties of the lens, the narrow band-pass filter and the detector are 0.8 %, 2.4 % and 2 % respectively. With these values the total uncertainty is calculated to be 31.4 %. For this source a current uncertainty of 31.4 % results in a temperature uncertainty of 10.1%. At an operational temperature of 2200 K this is ± 222 K.

Without the narrow band-pass filter the error is much larger, because the uncertainties for one specific wavelength can be better estimated than the uncertainties for the entire sensitivity spectrum of the detector. As it is more difficult to calculate this uncertainty for the entire spectrum and the uncertainty varies per wavelength, an uncertainty of 50 % in the current measurement has been used. This results in a temperature uncertainty of 14.2 %.

For the dual wavelength setup the uncertainties relating to the dimensions are not important anymore, but the large emissivity error is still present. Calculating the uncertainty using the same values as described in section 3.4.3 results in an current measurement uncertainty of 9.0 %. This translates to an uncertainty in the temperature of 8.26 % in the range of interest around 2200 K. At 2200 K this corresponds to an uncertainty of 198 K. Nonetheless, the unknown variations in the emissivity in combination with the losses of transmission through the enclosure will likely impact both wavelengths in a similar way, thereby reducing the error.

3.7.3 CCD camera setup

An initial experiment has been done to verify the feasibility of using a CCD camera. For this, a FLIR Dragonfly2 FireWire 400 (1394a) camera has been placed in front of the viewing window as was described in figure 2.9. An optical density filter, ND 0.9, has been placed in front of the lens to avoid saturation based on the exposure settings with minimal software gain. As was mentioned before, the biggest advantage is that alignment can be done very precisely as the target is imaged on

the computer. Figure 3.20 shows a digitally zoomed-in image of the tantalum emitter taken with the camera. The circular emitter is visible in white and what looks like Saturn's rings, the pointy white shapes pointing in the upper right and bottom left directions, is the glow of the support structure of the emitter. These supporting legs were shown in figure 3.8. The emitter does not change shape or position during operation, so a longer integration time can be used to create a good signal.

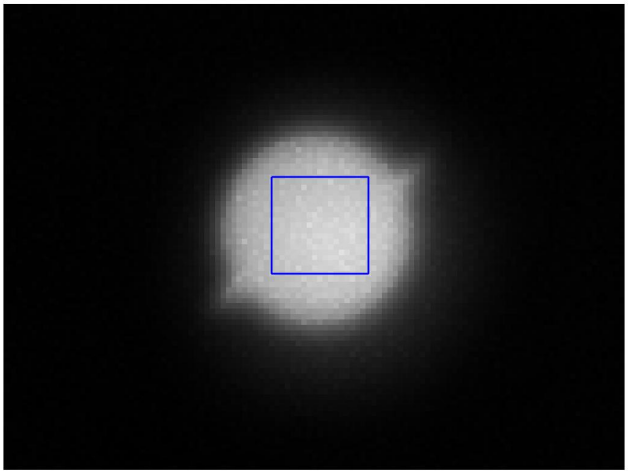

Figure 3.20: An image by a CCD camera of the emitter at high temperature. The blue square indicates the area that is used for the intensity measurements.

The intensity is measured by averaging the values of the pixels of the emitter that are within the blue square that is visible in figure 3.20. This way the supporting legs and the glow around the edges are filtered out. Another benefit of using a CCD chip is that it creates an x-y grid of pixels and thereby creating a heat map of the emitter.

Chapter 4

Results and Discussion

This chapter starts with the results of the preliminary experiments that were done with the single band pyrometer configuration in section 4.1. Then the results of the dual wavelength pyrometer configuration are discussed in section 4.2. At last, the initial results of using a CCD camera for the temperature measurements are shown in section 4.4.

4.1 Test setup results

4.1.1 Single band pyrometer

The temperature of the quartz tungsten-halogen lamp is measured by looking at the intensity over the entire sensitive range of the detector and with the 1550 nm narrow band-pass filter. The filament is supposed to have a temperature of approximately 2500 K during operation according to the manufacturer, but no uncertainty data is given. Figure 4.1 indicates what current is expected as a

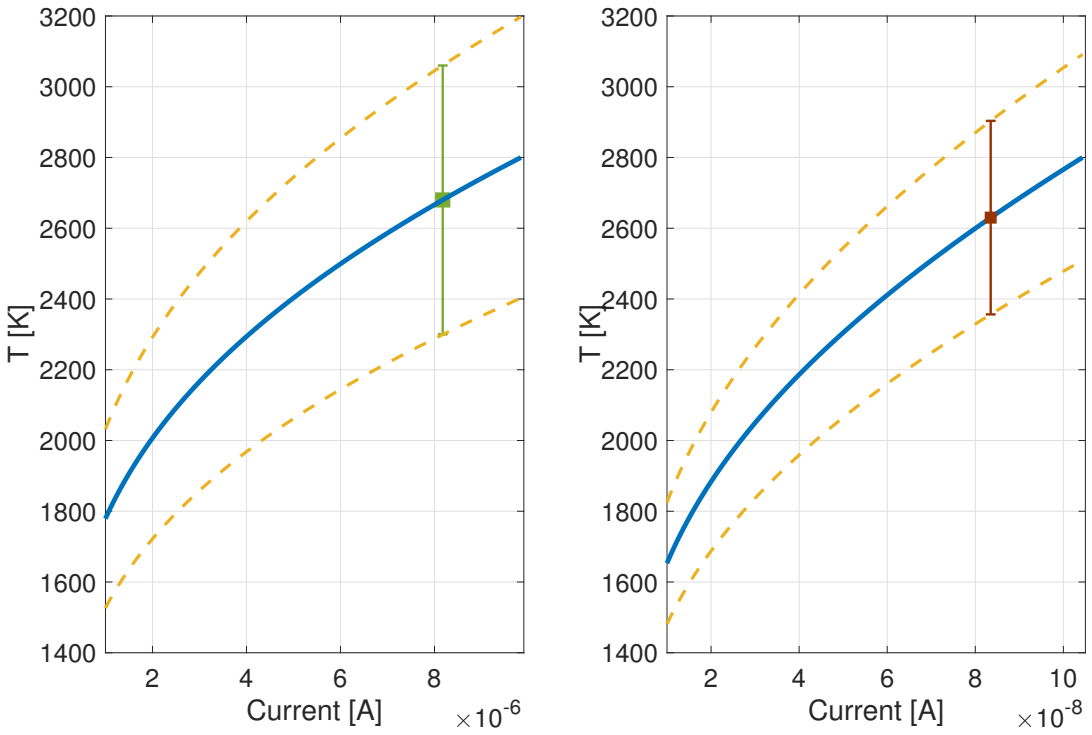

Figure 4.1: The temperature is plotted for a range of detector signals. On the left the signal of a photodiode detector with no band-pass filter in front of it and on the right the calculated signal when using a 1550 nm narrow band-pass filter in front of the detector. The green and red squares indicate the measured current values on the x-axis and their corresponding temperatures on the y-axis.

function of the temperature of the tungsten filament for both 1550 nm only and the full detector range. As the temperature goes up both signals increase non-linearly. The error of this method is largest, because the dimensions of the system and its uncertainty have to be taken into consideration.

Using the 1550 nm narrow band-pass filter, the current was measured to be 82 nA ± 25.7 nA, which is indicated by the red square in figure 4.1. The corresponding error of 10.1 % is shown in figure 4.1 as well by the yellow dotted lines above and below the blue solid line. A current of 82 nA ± 25.7 nA translates to a temperature of 2630 K ± 266 K. Using the complete range of the detector gives a 8.3 µA signal ± 4.15 µA, which is indicated by the green square in figure 4.1, which is equal to 2680 K ± 381 K. As this uses the entire sensitive range of the photodiode and therefore includes more uncertainties, the error is larger than using the 1550 nm band-pass filter. For example, the emissivity is considered constant across 900 to 1700 nm due to the lack of known emissivity values, though it is more likely to vary across different wavelengths. Also, the model assumes exact cut-offs at 900 and 1700 nm (figure 3.11d), whereas this varies for the detector in the experiment. Both of these uncertainties are too large to use the methods for the temperature measurement of the emitter inside the gun housing.

4.1.2 Dual wavelength pyrometer

Using the dual wavelength pyrometer setup, the same near infrared light of the small tungsten filament inside a Thorlabs housing was captured. Figure 4.2 shows the intensity ratios of the dual wavelengths plotted versus the temperature of the tungsten wire. After the light source had time to warm up for 20 minutes, the measured ratio was 1.77 with an uncertainty of 9.0 %, which is indicated by the blue square in figure 4.2. This corresponds to a temperature of 2450 K with an uncertainty of 8.3 %, meaning ±203. This is close to and in the range of the specifications supplied by Thorlabs. In the next section this setup will be used in combination with the tantalum emitter inside the thermionic gun vessel.

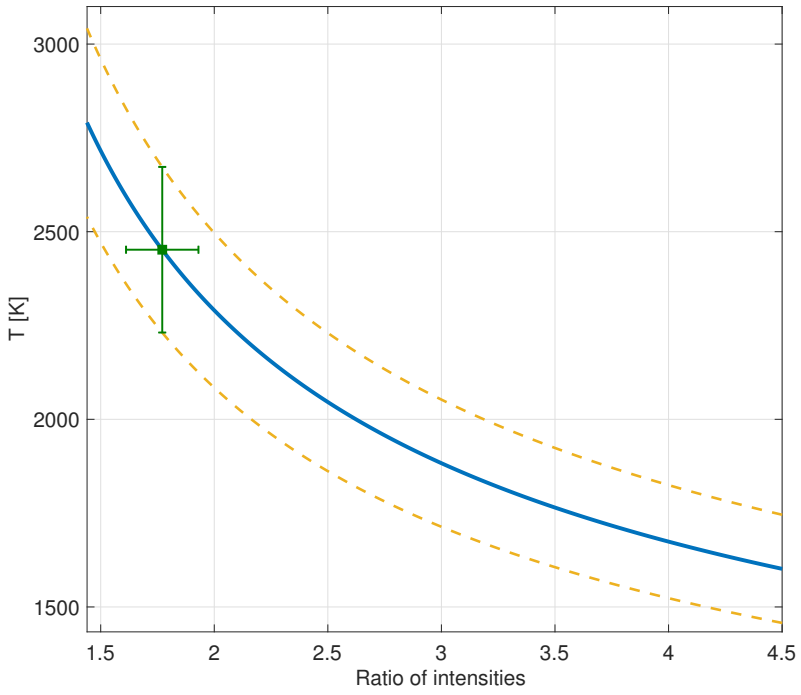

Figure 4.2: The ratios of the intensities plotted versus the temperature of the Quartz tungsten-halogen source. The uncertainty margin is indicated by the yellow dotted lines and the measured ratio is indicated by the green square.

4.2 Measurements during gun operation

The first measurements of the temperature of the emitter have been done using the tantalum emitter. The optical setup used is shown in figure 3.10. The LaB_6 emitters could not be placed inside the setup yet, so instead the tantalum emitter was used. It does not have a guard ring like the LaB_6 emitter has, but in combination with a 50 µm aperture the setup functions similarly. Future use of the LaB_6 emitter is described in section 6.2.

4.2.1 Tantalum emitters

The used tantalum emitters are described in section 3.2.1. Most important for the tantalum emitter is that a heating current somewhere from 1.4 A up to 1.8 A is needed to reach a filament temperature of 2200 K and an emission current of 1 mA. An image of a tantalum emitter can be seen in figure 3.8. As the tantalum emitter has no guard ring like the LaB_6 emitter does, there is no need for a small aperture and the full 0.82 mm (diameter) can be imaged.

The emissivity of tantalum with a polished surface is 0.47 for 1050 nm and 0.43 for 1550 nm, as is stated in literature[41]. With these values the expected temperature corresponding to the ratios of the both wavelengths was calculated. This is done using the known transmission values of the optical components, the emission properties of the material and the sensitivity of the detectors, all of which is described in section 3.10. Figure 4.3 shows the expected temperature for the ratios of the intensities of the wavelengths. The typical operational temperature of 2200 K corresponds to a measured ratio of 2.15.

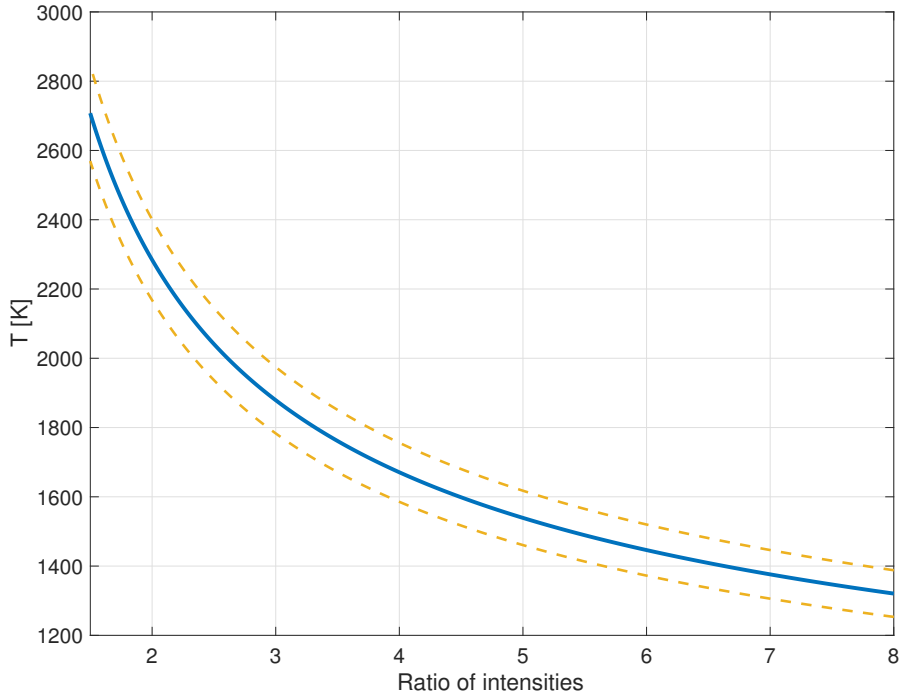

Figure 4.3: The calculated temperature of the tantalum emitter is plotted as a function of the ratios of the intensities of the 1550 nm and 1050 nm emitted wavelengths. The uncertainty of ±4.7% is indicated by the yellow dotted lines.

The temperature of the emitter can be plotted as a function of the heating current. This is shown in figure 4.4 with a 4.7 % temperature uncertainty. As the heating current passes 1.3 A, the temperature of the emitter is above 2100 K and is expected to reach 2200 K at about 1.4 A. This

corresponds to the typical operation temperature specified by the supplier. As the heating current gets close to 1.4 A, the tantalum emitter started emitting electrons with a current in the order of μA, which increased as the heating current increased. There was no electric field present, so the electrons could not be accelerated to keV energies. To make sure not to break the support structure, and therefore the emitter, by operating above the operational limit, the measurements were stopped here.

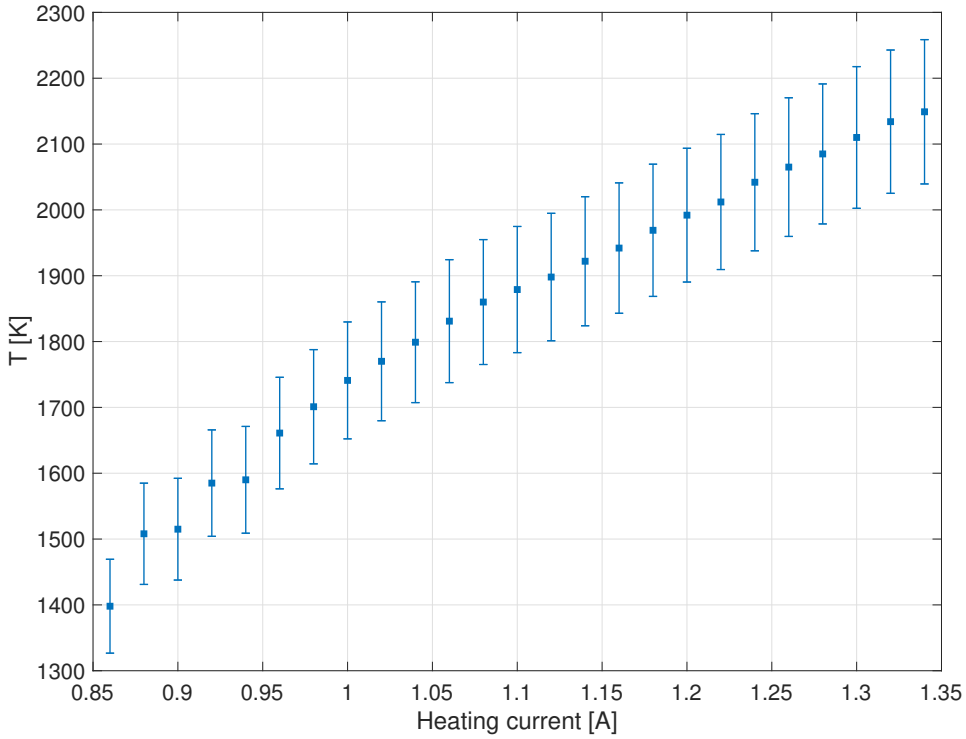

Figure 4.4: The temperature of the tantalum emitter as a function of the heating current.

4.2.2 LaB_6 imitation

The real LaB_6 emitter could not be used yet as the setup was not ready for it. To imitate the smaller size and the focusing on the LaB_6 part within the emitter surface, the tantalum emitter has been used in combination with an aperture. The magnification of the emitter at the image plane after the first bi-convex lens is calculated to be 0.27x. With an object size of 300 μm for the original LaB_6 emitter, the image size will be 81 μm at the image plane where the aperture is located. Therefore an aperture with a diameter of 50 μm is used to see only the center part of the emitter. Alignment was done using a FLIR CCD camera to make sure the aperture is exactly in the focus point of the first lens. Figure 4.5 shows an image of the aperture taken during alignment. From there it has to be shifted by a distance of 1.46 mm using a translation stage to account for the chromatic aberrations if used for the 1550 nm current measurement.

The aperture blocks most of the incoming light, letting through only a fraction of it. The light eventually reaching the detectors generated a stable current signal of around 2 nA after zero-correction. The ratios of the measured intensities varied significantly, around ± 65 % depending on the alignment due to the 50 μm aperture. Figure 4.6 shows the temperature as a function of the heating current. The uncertainty in the temperature is much larger and estimated to be 30 % due to the spread in the data after different alignments. It can be seen that the measured ratios lead to temperatures that are generally higher than the temperatures seen in figure 4.4. This makes the current setup unusable for reliable temperature measurements that are needed for operation at an emitter temperature of 1760 K. The deviation over the different measurements is likely a result of the alignment errors in

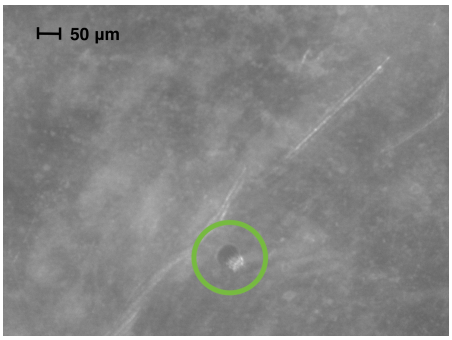

Figure 4.5: A picture by a FLIR CCD camera of the 50 µm aperture (indicated by the green circle). When the aperture is in focus, as is the case here, the aperture and the image plane of the first lens are aligned.

combination with the chromatic aberrations at the image plane where the aperture is located (see figure 3.14).

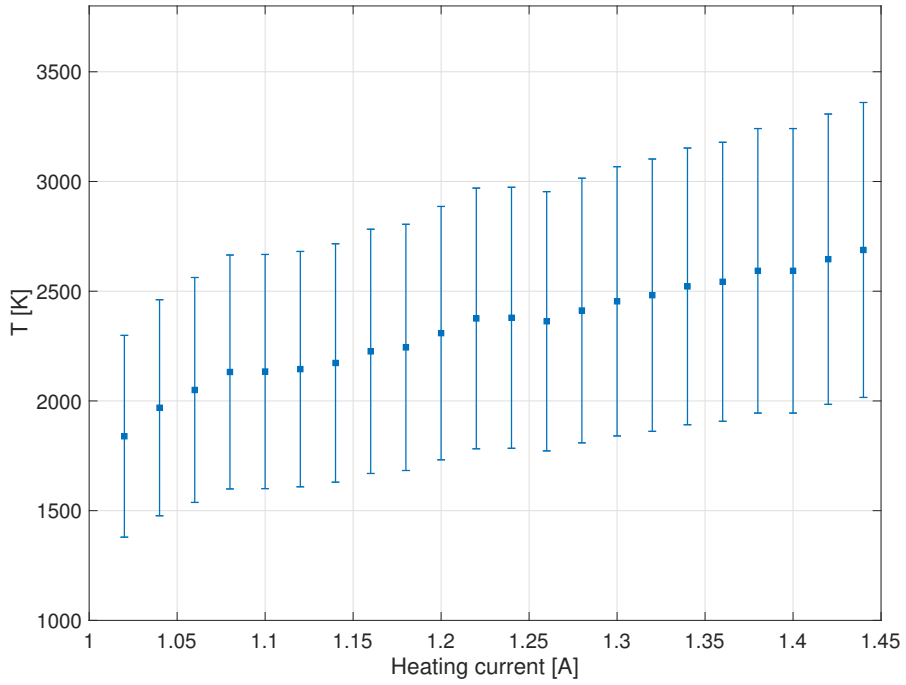

Figure 4.6: The heating current of the tantalum emitter plotted versus the temperature of the emitter, determined with the corresponding measured intensity ratios of the 1550 nm and 1050 nm light.

4.3 Radiation

The biggest limitation during the experiments was the unexpectedly high amount of x-ray radiation coming from where the electrons hit the Faraday cup and the gold-plated mirror. The lowest setting for the emission current of the power supply is 3 µA. At a potential of -60 kV applied to the emitter and an emission current of 3.8 µA the radiation dose was measured to be 500 µSv/hr at a distance of approximately 7.5 cm from the Faraday cup, measured perpendicular to the propagation direction of the electron beam. This is illustrated in figure 4.7. The amount of radiation at 3.8 µA is already above the safety limits that need to be followed in order to safely conduct experiments. To achieve an electron beam current of 10 mA, the emission current would need to be increased by a factor of almost 3000. The complete beam line will then need shielding to guarantee safety during future

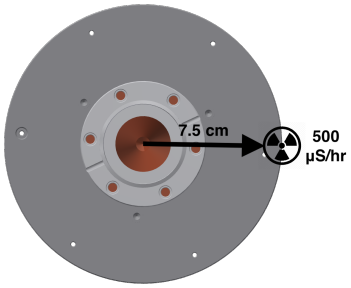

Figure 4.7: Depiction of where the radiation was measured with respect to the Faraday cup and the electron beam line. At the indicated point 7.5 cm from the beam line, he radiation was measured to be 500 µS/hr.

operation at any beam current used.

Simply switching between setting is not the same as using optical density filters, as the dark current and internal noise will affect the signal when settings are changed.

4.4 Experiments with the CCD camera

Using the setup described in sections 2.3.8 and 3.7.3, the relative intensity of the emitter can be measured of the heating current of the emitter. This is shown in figure 4.8 for three different tries with the same exposure settings.

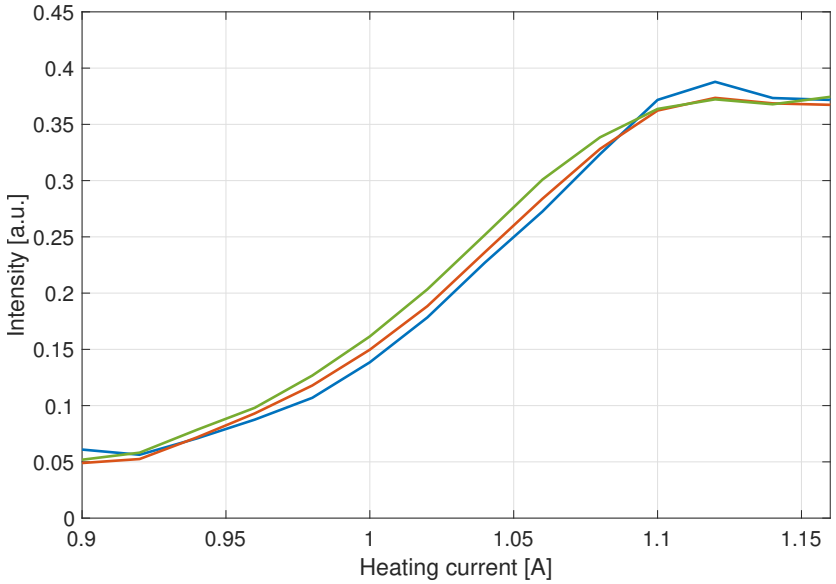

Figure 4.8: The intensity of the electron emitter measured by the CCD camera as a function of the heating current.

It can be seen that as the heating current goes up, the measured intensity goes up as was expected. At around 1.1 A the camera is saturated and the intensity does not increase any further. This shows that the dynamic range of the CCD chip of the camera is too low to use for this emitter. Using different exposure settings to extend the dynamic range across measurements changes the effect of dark current and signal noise. It is possible to work with multiple optical density filters, but that makes the measurement procedure more complex. Furthermore, for this camera the reproducibility of the measured intensity is not stable enough to give a reliable measurement as it varies by around

10 % over different measurements using the same exposure settings. Better results are expected to be achieved using a camera with red, green and blue pixels as that would also give the relative differences between the intensities at different wavelengths instead of one intensity signal. Nonetheless, both the monochromatic camera and the rgb camera would need to be absolutely calibrated before they can be used. With the information displayed in figure 4.8 no temperature information can be deduced, nor the corresponding uncertainty.

Chapter 5

Conclusion

The first phase of the development of the 100 kV thermionic gun has been successfully built, which includes the gun vacuum vessel with a ta emitter installed, a mirror in the beam line with the optical setup attached to it and the water-cooled Faraday cup to stop the beam. Temperature measurements were carried out using dual wavelength pyrometry in a setup that allows taking temperature measurements during operation. For the tantalum emitter the temperature can be determined by looking at the ratio of the intensities of 1550 nm and 1050 nm light that it emitted, but the current setup has a temperature uncertainty of 4.7 % without calibration. This is above the required error of 2.27 % at an operational temperature of 1760 K. Using single band pyrometry for the temperature measurement is also possible, but this results in a larger uncertainty and the calibration is more difficult. In case of the test setup, it had a temperature uncertainty of 10.1 %, though this is mostly due to the uncertainty of the used source in the test setup. In the future scenario of a LaB_6 cathode with a smaller emission surface surrounded by a carbon guard ring, an aperture of around 50 µm is required. The aperture is used to separate the emission surface from the guard ring, because they have different emission spectra and because there exists a temperature difference of about 20 K. However, the lenses used in the setup introduced chromatic aberrations when focusing the image onto the aperture. Due to the difference of 1.46 mm in the imaging distances between 1050 nm and 1550 nm when using a bi-convex lens, the chromatic aberrations are too large for using a 50 µm aperture. This affected the ratio of the two intensities in such a way that the temperature could not be related to the measured ratio of intensities anymore using the predicted values. Aside from the chromatic aberrations in case of the LaB_6 cathode, the main sources of error were the alignment of the optical components and the unknown emissivity values, especially for the tantalum cathode. As alignment with a sub 100 µm aperture is difficult, the measurement could be done using a CCD camera when the calibration setup is in place. This way the emission area, and thus its measured intensity, can be easily chosen from the image that is seen on the computer. Initial experiments have shown that using a CCD camera does require the use of multiple optical density filters as the dynamic range of the chip does not cover the entire range of black body intensities of the emitter and will saturate.

The mentioned uncertainties can be reduced by using a calibration setup that involves measuring the absolute temperature of another piece of the same emitter material using a type B thermocouple. By building this into the existing beam line, the dual wavelength pyrometer setup can be calibrated after alignment. Calibrating after alignment means the systematic uncertainty in the optical losses and the aberrations of the optical components can be eliminated. Also, using the same emitter material in the calibration takes away the emissivity uncertainty. In this scenario the uncertainty is dictated by the error of the thermocouple, which is 0.25 % assuming good thermal contact.

During the time of this report the emission current was limited to currents below the lowest emission current setting of the power supply of 3 µA. This limitation was due to the amount of radiation that was produced, which was higher than is allowed by the safety regulations. Proper shielding is currently being implemented, so the measurements can take place with higher current operation up to 10 mA. With the temperature measurements done at higher currents, the temperature that is measured using the dual wavelength pyrometer can be compared to the temperatures that are expected using the Richardson's equation and the measured emission current.

After 10 mA has been achieved, another LaB_6 cathode with a larger emitter area will be used. A larger emitting area will improve the signal to noise ratio and make alignment easier with a larger aperture.

Chapter 6

Outlook

In this report only the first steps in the development of the thermionic gun operation have been discussed. There is more to come and therefore this chapter looks forward and discusses what will be relevant for future experiments.

6.1 Achromatic lenses

One of the most limiting factors for the LaB_6 measurements are the chromatic aberrations (section 3.5) caused by the first bi-convex lens, lens 1. In order to improve the accuracy without calibration and make the measurement procedure less complex, Achromatic Doublets from Thorlabs with the same coating can be used in combination with a different wavelength selection[42]. Figure 6.1 shows the focal length shift for different wavelengths ranging from 1050 nm to 1700 nm. When choosing wavelength combinations such as 1050 nm and 1400 nm or 1100 nm and 1330 nm, the focal length difference between the two is 0, thus eliminating the chromatic aberrations. These wavelength combinations might be less favorable due to reasons mentioned in section 3.4.2, but it solves the most challenging limitation of the current calibration-less setup.

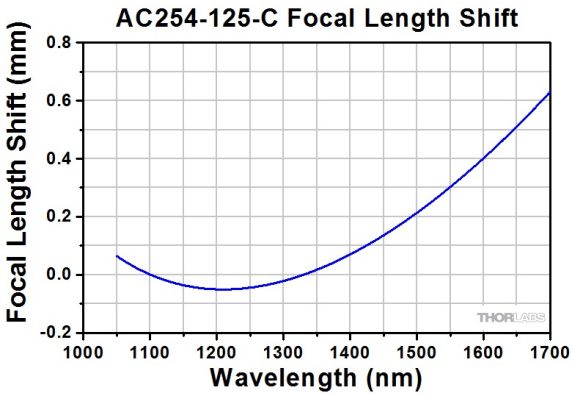

Figure 6.1: The focal length shift as a function of the wavelength for a specific selection of Thorlabs lenses[42].

6.2 LaB_6 experiments

When the lab conditions are such that the LaB_6 cathode can be used, the temperature of the LaB_6 cathode can be determined and measured as a function of the heating current. By slowly heating the LaB_6 cathode without the 100 kV bias applied to it, as was done for the tantalum cathode, the measured temperature can be compared to the supplied dataset of the manufacturer AP Tech. This dataset is shown in figure 6.2 and shows the temperature of a specific LaB_6 cathode as a function of the power supplied by the power supply. This data varies per LaB_6 emitter.

The second way to verify whether the dual wavelength pyrometry measurements are in the correct

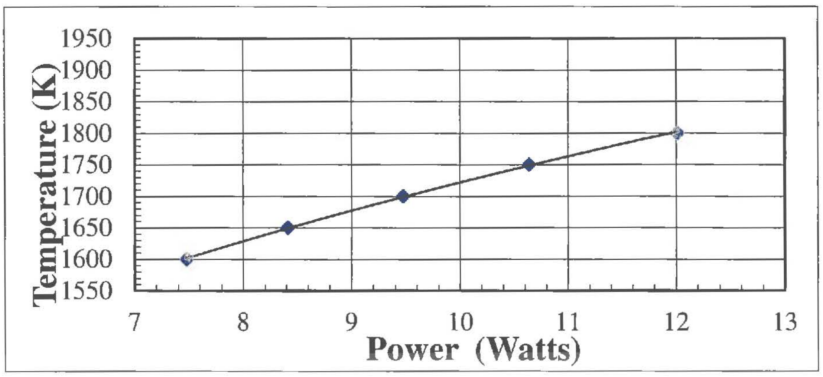

Figure 6.2: AP Tech data on the temperature of the LaB_6 electron emitter as a function of the supplied power.

range is to compare the measured temperatures using the Richardson-Dushman equation. Equation 2.4 shows the Richardson-Dushman equation that is corrected for the Schottky effect and can be used to determine the emitter temperature based on the measured emission current. This can only be done when thermionic emission is possible in the lab. In figure 6.3 the emission current from the LaB_6 cathode is plotted versus the theoretical temperature determined by the Richardson-Dushman equation. The emission current is monitored by both the power supply and through measurements using the Faraday cup at the end of the beam line.

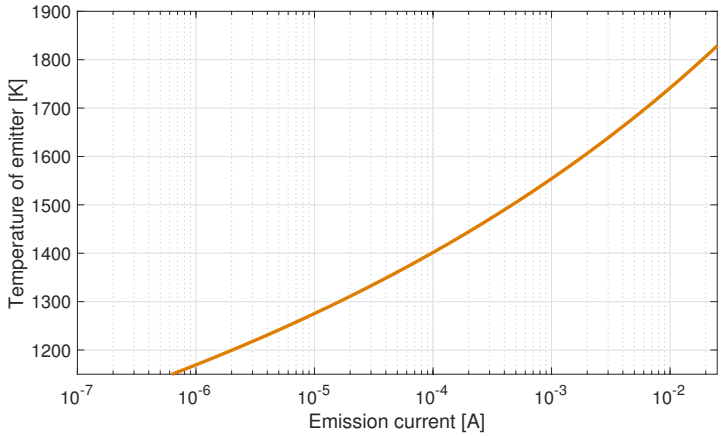

Figure 6.3: The temperature of LaB_6 emitter plotted as a function of the emission current based on the Richardson's equation with the Schottky effect.

6.3 High current operation

The end goal is to develop a thermionic gun that can be used as an injector for free electron lasers or inverse Compton scattering sources. To compete with other electron injectors, such as the Cornell gun and the SACLA gun, the number of electrons, or the charge per bunch, needs to go up while maintaining a small beam emittance and a high repetition rate[13].

After the current setup is expanded with the chopper and buncher RF cavities and reaches its desired bunched electron beam output, it can be prepared for high current operation. The power supply that is used in the current setup can supply only up to 10 mA and therefore the current electron emitter is designed for this output. Moving towards a higher current, about 250 mA, requires a more powerful power supply, an electron emitter with a larger surface or operation using different parameters, e.g. reaching higher filament temperatures.

Manufacterer	Emitter material	Work function (eV)	Ag	d [mm]	T [K]	Emission current [A]	Emittance [m rad]
A-P-Tech	LaB6 with guard (used)	2.7	29	0.3	1800	0.0187	4.13e-8
A-P-Tech	LaB6	2.7	29	2.8	1800	1.62	3.86e-7
Kimball Physics	ES-440 (High Current) LaB6	2.7	29	1.78	1900	1.76	2.52e-7
Kimball Physics	LaB6 with guard	2.7	29	0.25	1900	0.0346	3.54e-8
3M	Tungsten impregnated	1.8	3	3	1200	0.126	3.38e-7
Kimball Physics	Tantalum	4.1	60	1.57	2200	0.0209	2.44e-7
A-P-Tech	HfC with guard	3.58	120	1	1900	0.011	1.41e-7

Table 6.1: Overview of different cathodes and their theoretical output values.

When going to a more powerful power supply, it is recommended to choose one with a slight overcapacity (in the order of several kV). The electron gun is experimentally found to be more stable when it is trained for slightly higher voltages as compared to training it only to its operational maximum. Training in this case means increasing the voltage on the cathode in small steps to arc away any impurities on the surface of the anode and cathode around it.

As can be seen from equation 2.1, the emission current depends on a material specific constant, the radius of the emitter, the temperature at which it is operated and the work function of the material. A comparison has been done to compare different materials and emitter sizes to create an overview of what can be upgraded in the future.

The only available cathodes reaching emission currents of 250 mA and higher are LaB_6 cathodes. Both AP Tech and Kimball Physics provide these and their sizes can be scaled down to reduce emittance. Also, the maximum operational temperature has a large impact on the emission current that can be achieved.

Bibliography

[1] B.W.J. Mcneil and N.R. Thompson. X-ray free-electron lasers. *Nature Photonics*, 4(12):814–821, 2010. 1

[2] X. Stragier. Thermionic electron source as injector for a high power, high repetition rate Free Electron Laser. (January), 2016. 1

[3] F. Sannibale. Overview of recent progress on high repetition rate, high brightness electron guns. *IPAC 2012 - International Particle Accelerator Conference 2012*, pages 4160–4164, 2012. 1, 2, 3

[4] P Emma, R Akre, J Arthur, R Bionta, C Bostedt, J Bozek, A Brachmann, P Bucksbaum, R Coffee, F.-J. Decker, Y Ding, D Dowell, S Edstrom, A Fisher, J Frisch, S Gilevich, J Hastings, G Hays, Ph. Hering, Z Huang, R Iverson, H Loos, M Messerschmidt, A Miahnahri, S Moeller, H.-D. Nuhn, G Pile, D Ratner, J Rzepiela, D Schultz, T Smith, P Stefan, H Tompkins, J Turner, J Welch, W White, J Wu, G Yocky, and J Galayda. First lasing and operation of an ångstrom-wavelength free-electron laser. *Nature Photonics*, 4(9):641–647, 2010. 1

[5] L. Zheng, Z. Li, Y. Du, H. Chen, B. Gao, R. Li, and W. Huang. Design of a 217 MHz VHF gun at Tshingua University. pages 1–4. 1

[6] O.J. Luiten. *KNAW-Agenda Grootschalige Onderzoeksfaciliteiten : Smart*Light: a Dutch table-top synchrotron light source*. Koninklijke Nederlandse Akademie van Wetenschappen (KNAW), 10 2016. Eervolle vermelding van de KNAW-commissie. 1

[7] W.F. Toonen, X.F.D. Stragier, P.H.A. Mutsaers, and O.J. Luiten. Gigahertz repetition rate thermionic electron gun concept. *Phys. Rev. Accel. Beams*, 22:123401, Dec 2019. 2, 4, 9, 23, 24

[8] R. Wells, W. Ghiorso, J. Staples, T. Huang, F. Sannibale, and T. Kramasz. Mechanical design and fabrication of the vhf-gun, the berkeley normal-conducting continuous-wave high-brightness electron source. *Review of Scientific Instruments*, 87:023302, 02 2016. 2

[9] D. Janssen, H. Bttig, P. Evtushenko, M. Freitag, F. Gabriel, B. Hartmann, U. Lehnert, P. Michel, K. Mller, B. Reppe, A. Schamlott, C. Schneider, R. Schurig, J. Teichert, S. Konstantinov, S. Kruchkov, A. Kudryavtsev, O. Myskin, and C. Haberstroh. First operation of a superconducting rf-gun. *Nuclear Instruments and Methods in Physics Research Section A: Accelerators, Spectrometers, Detectors and Associated Equipment*, 507:314–317, 07 2003. 2

[10] L. Cultrera. Cathodes for photoemission guns. *Proceedings of 2011 Particle Accelerator Conference, New York, NY, USA*, 2011. 2

[11] H. Qian and E. Vogel. Overview on cw rf gun developments for short wavelength fels. *39th International Free-Electron Laser Conference, Hamburg, Germany*, Aug 2019. 3

[12] C. Gulliford, A. Bartnik, I. Bazarov, B. Dunham, and L. Cultrera. Demonstration of cathode emittance dominated high bunch charge beams in a DC gun-based photoinjector. *Applied Physics Letters*, 106(9), 2015. 3

[13] K. Togawa, T. Shintake, T. Inagaki, K. Onoe, T. Tanaka, H. Baba, and H. Matsumoto. CeB6 electron gun for low-emittance injector. *Physical Review Special Topics - Accelerators and Beams*, 10(2):1–10, 2007. 3, 56

[14] O.W. Richardson. The emission of electricity from hot bodies. 1921. 7

[15] O.W. Richardson. Electron Emission from Metals as a Function of Temperature. *Physical Review*, 23(2):153–155, Feb 1924. 7

[16] C.R. Crowell. The richardson constant for thermionic emission in schottky barrier diodes. *Solid-State Electronics*, 8(4):395399, 1965. 7, 8

[17] E.L. Murphy and R.H. Good. Thermionic emission, field emission, and the transition region. *Phys. Rev.*, 102:1464–1473, Jun 1956. 9

[18] P. Buffat, 2007. 9

[19] C.D. Child. Discharge from hot cao. *Phys. Rev. (Series I)*, 32:492–511, May 1911. 9

[20] K. Torgasin, K. Morita, H. Zen, K. Masuda, T. Katsurayama, T. Murata, S. Suphakul, H. Yamashita, T. Nogi, T. Kii, and et al. Thermally assisted photoemission effect on ceb6 and lab6 for application as photocathodes. *Physical Review Accelerators and Beams*, 20(7), 2017. 10

[21] Lanthanum hexaboride info. http://www.a-p-tech.com/lab6-cathodes.html. Accessed: 2019-27-04. 11, 31

[22] Torsten Lundstrom. Structure, defects and properties of some refractory borides. *Pure and Applied Chemistry*, 57(10):13831390, Jan 1985. 11

[23] Lanthanum hexaboride (lab6) picture. https://www.samaterials.com/lanthanum/1414-lanthanum-hexaboride-lab6-tube.html. Accessed: 2019-27-04. 11

[24] P.R.N. Childs, J.R. Greenwood, and C.A. Long. Review of temperature measurement. *Review of Scientific Instruments*, 71(8):2959–2978, 2000. 12

[25] R.S.M. Chrystie, Omid M. Feroughi, Thomas Dreier, and Christof Schulz. Sio multi-line laser-induced fluorescence for quantitative temperature imaging in flame-synthesis of nanoparticles. *Applied Physics B*, 123(4):104, Mar 2017. 13

[26] L. Boltzmann. Ableitung des stefan'schen gesetzes, betreffend die abhngigkeit der wrmestrahlung von der temperatur aus der electromagnetischen lichttheorie. *Annalen der Physik*, 258(6):291–294, 1884. 13

[27] G.K. Burgess. *Pyrometers: The Measurement of High Temperatures*. Engineering Instrumentation Series. Wexford College Press, 2006. 13

[28] G.B. Rybicki and A.P. Lightman. *Radiative processes in astrophysics*. WILEY-VCH, 2004. 14

[29] M.J. Moran, H.N. Shapiro, D.D. Boettner, and M.B. Bailey. *Fundamentals of engineering thermodynamics*. Wiley, 2019. 15

[30] Williams pyrometer wavelength selection guide. https://www.williamsonir.com/pyrometer-wavelength-selection-guide/. Accessed: 2019-02-09. 15

[31] N-bk7 ar coating: 1050 - 1700 nm information. https://www.thorlabs.com/newgrouppage9.cfm?objectgroup_id=4850. Accessed: 2019-27-04. 16, 34, 35

[32] J.M.D. Kowalczyk, M.R. Hadmack, E.B. Szarmes, and J.M.J. Madey. Emissivity of lanthanum hexaboride thermionic electron gun cathode, 2014. 21, 22

[33] F.R. Connor. *Wave transmission*. Edward Arnold, 1985. 23

[34] Mini vogel mount by applied physics technologies. http://www.a-p-tech.com/mini-vogel-mount.html. Accessed: 2019-27-04. 30

[35] Tantalum disk cathodes by kimball physics. https://www.kimballphysics.com/ta-discs. Accessed: 2019-02-09. 31

[36] Longpass dichroic mirrors/beamsplitters. https://www.thorlabs.com/newgrouppage9.cfm?objectgroup_id=3313. Accessed: 2019-27-04. 32, 33, 34

[37] Nir bandpass laser line filters: 700 - 1650 nm center wavelength. https://www.thorlabs.com/newgrouppage9.cfm?objectgroup_id=1000. Accessed: 2019-27-04. 34

[38] Free-space biased detectors. https://www.thorlabs.com/newgrouppage9.cfm?objectgroup_id=1295. Accessed: 2019-27-04. 34, 36

[39] Ultra high temperature probes. https://www.vulcanelectric.com/products/ultra-high-temp-probes/. Accessed: 2019-27-04. 40

[40] L. Bloomfield. *How everything works: making physics out of the ordinary*. Wiley, 2008. 41

[41] Y.S. Touloukian and D.P. DeWitt. *Thermophysical Properties of Matter - The TPRC Data Series. Volume 7. Thermal Radiative Properties - Metallic Elements and Alloys*. Defense Technical Information Center, 1970. 47

[42] Unmounted achromatic doublets, ar coated: 1050 - 1700 nm thorlabs page. https://www.thorlabs.com/newgrouppage9.cfm?objectgroup_id=899. Accessed: 2019-02-09. 55